

Probing many-body noise in a strongly interacting two-dimensional dipolar spin system

Emily J. Davis,^{1,*} Bingtian Ye,^{1,*} Francisco Machado,^{1,2,*} Simon A. Meynell,³ Thomas Mittiga,^{1,2} William Schenken,³ Maxime Joos,³ Bryce Kobrin,^{1,2} Yuanqi Lyu,¹ Dolev Bluvstein,⁴ Soonwon Choi,¹ Chong Zu,^{1,2,5} Ania C. Bleszynski Jayich,^{3,†} and Norman Y. Yao^{1,2,‡}

¹*Department of Physics, University of California, Berkeley, CA 94720, USA*

²*Materials Science Division, Lawrence Berkeley National Laboratory, Berkeley, CA 94720, USA*

³*Department of Physics, University of California, Santa Barbara, CA 93106, USA*

⁴*Department of Physics, Harvard University, Cambridge, MA 02138, USA*

⁵*Department of Physics, Washington University, St. Louis, MO 63130, USA*

(Dated: March 25, 2021)

The most direct approach for characterizing the quantum dynamics of a strongly-interacting system is to measure the time-evolution of its full many-body state. Despite the conceptual simplicity of this approach, it quickly becomes intractable as the system size grows. An alternate framework is to think of the many-body dynamics as generating noise, which can be measured by the decoherence of a probe qubit. Our work centers on the following question: What can the decoherence dynamics of such a probe tell us about the many-body system? In particular, we utilize optically addressable probe spins to experimentally characterize both static and dynamical properties of strongly-interacting magnetic dipoles. Our experimental platform consists of two types of spin defects in diamond: nitrogen-vacancy (NV) color centers (probe spins) and substitutional nitrogen impurities (many-body system). We demonstrate that signatures of the many-body system’s dimensionality, dynamics, and disorder are naturally encoded in the functional form of the NV’s decoherence profile. Leveraging these insights, we directly characterize the two-dimensional nature of a nitrogen delta-doped diamond sample. In addition, we explore two distinct facets of the many-body dynamics: First, we address a persistent debate about the microscopic nature of spin dynamics in strongly-interacting dipolar systems. Second, we demonstrate direct control over the spectral properties of the many-body system, including its correlation time. Our work opens the door to new directions in both quantum sensing and simulation.

Introduction

Understanding and controlling the interactions between a single quantum degree of freedom and its environment represents a fundamental challenge within the quantum sciences [1–18]. Typically, one views this challenge through the lens of mitigating decoherence—enabling one to engineer a highly coherent qubit by decoupling it from the environment [2–6, 8, 9, 19]. However, the environment itself may consist of a strongly interacting, many-body system, which naturally leads to an alternate perspective; namely, using the decoherence dynamics of the qubit to probe the fundamental properties of the many-body system [7, 10–16, 20, 21]. Discerning the extent to which such “many-body noise” can provide insight into transport dynamics, low-temperature order, and generic correlation functions of an interacting system remains an essential open question [22, 23].

By mapping the dynamics of a system onto the decoherence of a probe, one avoids the exponential complexity typically associated with many-body tomography [24, 25]. However, this efficiency comes at the cost of gathering less information. Nevertheless, by leveraging the toolset of non-equilibrium statistical mechanics, recent work has demonstrated that many-body noise spectroscopy can provide insight into a diverse array of physical phenomena, ranging from Cooper-paired super-

fluidity to quantum criticality and many-body localization [20, 21, 26–31].

On the experimental front, the idea of probing noise from a many-body system has a long tradition in the context of magnetic resonance spectroscopy [10–16]. Indeed, seminal work exploring the decoherence of paramagnetic defects in solids revealed the importance of many-body noise arising from strong dipolar interactions [10–16, 32]. Building upon this body of work, we first present a theoretical framework which both unifies and generalizes existing results regarding the decoherence of a probe coupled to a strongly-interacting, many-body system. In addition to solid-state spin systems, our framework naturally applies to a broader class of quantum simulation platforms, including trapped ions [33, 34], Rydberg atoms [35–37], and ultracold polar molecules [38].

Our framework predicts a non-trivial temporal profile for the average coherence of probe spins, which exhibits a crossover between two distinct stretched exponential decays [Fig. 1] [10–16, 32]. Crucially, we demonstrate—both theoretically and experimentally—that the associated stretch powers contain a wealth of information about both the static and dynamical properties of the many-body spin system. We focus on three particular properties. First, the stretch power can distinguish between different forms of spectral diffusion, shedding light on the nature of local spin fluctuations. Second, the

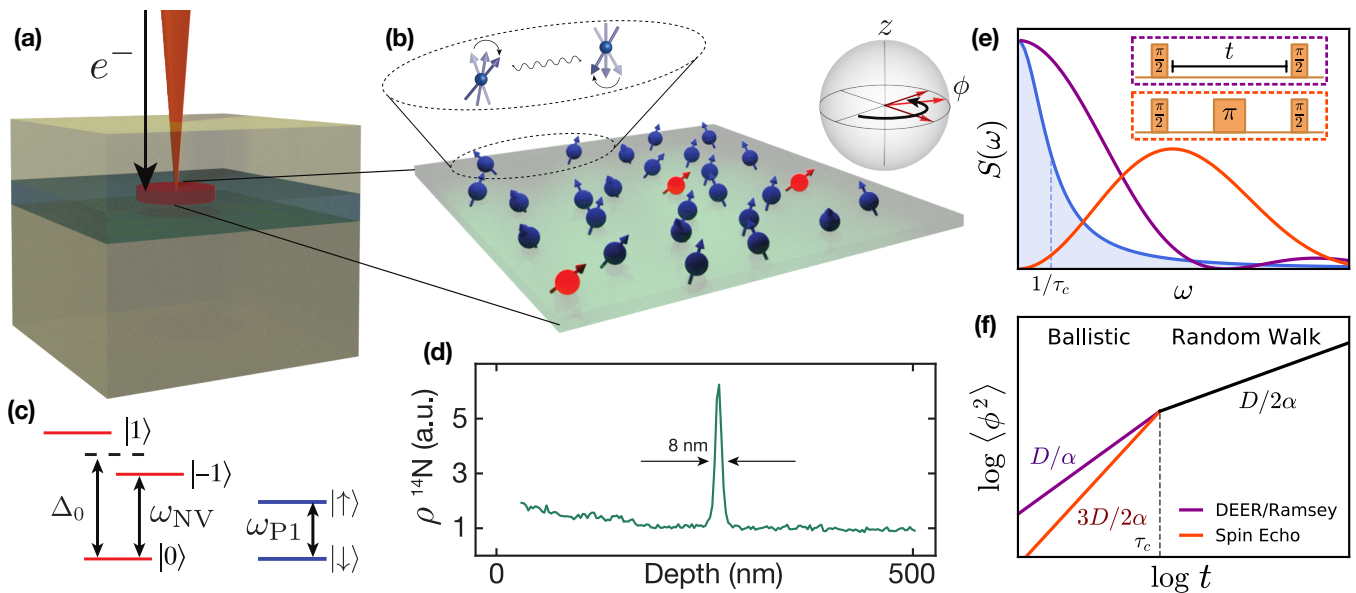


FIG. 1. (a) A delta-doped layer of ^{14}N (green) is grown on a diamond substrate. NV centers are created via local electron irradiation (orange beam) and subsequent high-temperature annealing. (b) Schematic depiction of a two-dimensional layer of NV (red) and P1 (blue) centers. Dilute NV centers function as probe spins of the dense, disordered P1 system. The P1s exhibit spin-flip dynamics driven by magnetic dipole-dipole interactions (zoom). Ising interactions with the P1 system cause the NV to accumulate phase, ϕ , during noise spectroscopy (Bloch sphere). (c) NV and P1 level structure in the presence of a magnetic field, B , applied along the NV axis. We work within an effective spin-1/2 subspace of the NV center, $\{|0\rangle, |-1\rangle\}$, with level splitting, ω_{NV} . The corresponding P1 splitting, ω_{P1} , is strongly off-resonant from the NV transition. (d) Secondary ion mass spectrometry (SIMS) measurement of the density of ^{14}N as a function of depth for sample S1. The presence of a 2D layer is indicated by a sharp Nitrogen peak with a SIMS-resolution-limited 8 nm width. (e) The overlap between the many-body spectral function (blue) and the power spectrum of the filter function $|f(\omega; t)|^2$ for both a Ramsey/DEER pulse sequence (purple) and a spin echo pulse sequence (orange) are shown. (f) Schematic depiction of the variance of the phase, $\langle \phi^2 \rangle = -2 \log C(t)$, as a function of the measurement duration t , for both Ramsey/DEER (purple) and spin echo (orange). The labeled slopes indicate the predicted stretch powers in both the early-time ballistic regime and the late-time random-walk regime [Table I]; the crossover occurs at the correlation time, τ_c .

crossover in time between different stretch powers allows one to extract the many-body system’s correlation time. Finally, the stretch power also contains direct signatures about the dimensionality and disorder intrinsic to the system.

This last point is particularly relevant given near-term prospects for engineering the dimensionality of spin systems embedded in solid-state platforms [39–41].

Indeed, while prior work in the solid-state has focused on dipolar spin ensembles in three dimensions [10–16, 32, 42], recent advances in materials growth have enabled the creation of two-dimensional *layers* of optically-active spin defects [39–41]. By combining nitrogen delta-doping during growth with local electron irradiation [39–41], we fabricate a diamond sample (S1) where paramagnetic defects are confined to a thin layer [Fig. 1(a, b)]. This layer contains a hybrid spin system consisting of two types of defects: spin-1 nitrogen-vacancy (NV) centers and spin-1/2 substitutional nitrogen (P1) centers. The dilute NV centers can be optically initialized and read-out, making them a natural probe of the many-body noise generated by the strongly-interacting P1 centers.

Even once created, the non-destructive, *in situ* characterization of the effective “dimensionality” of our sample (i.e. whether the average spin-spin spacing is larger than the thickness of the layer) is challenging with conventional methods. To this end, we demonstrate how the decoherence dynamics of NV probes can be used to prove the two-dimensional nature of the P1 ensemble; we compare these results to measurements on a conventional three-dimensional ensemble.

Next, we show that the stretch power of the NV centers’ coherence decay also reveals information about the nature of the many-body noise generated by the P1 system [11, 12, 14]. In particular, we demonstrate that the spin-flip dynamics are inconsistent with the conventional expectation of telegraph noise, but rather follow that of a Gauss-Markov process [Table I].

Finally, we actively control the noise spectral density of the many-body P1 system via polychromatic driving [43]. In particular, we directly tune the correlation time of the P1 system and measure a corresponding change in the crossover timescale between coherent and incoherent spin dynamics [14, 44].

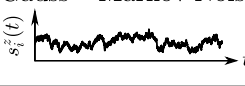
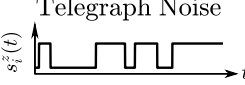
Many-Body Noise Properties	Measurement Sequence	Early-time (ballistic regime) stretch power	Late-time (random walk regime) stretch power
Gauss – Markov Noise 	DEER/Ramsey	D/α	$D/2\alpha$
	Spin Echo	$3D/2\alpha$	$D/2\alpha$
Telegraph Noise 	DEER/Ramsey	D/α	$D/2\alpha$
	Spin Echo	$1 + D/\alpha$	$D/2\alpha$

TABLE I. Predicted early and late-time stretch powers of the probe spin decoherence profile when coupled to a D -dimensional system via power-law Ising interactions $\sim 1/r^\alpha$. We distinguish between Gaussian and telegraph spin-flip noise in the many-body system, which gives rise to different predictions for the early-time spin echo stretch power.

Theoretical framework for decoherence dynamics induced by many-body noise

Let us begin by providing a framework for understanding the decoherence dynamics of probe spins coupled to an interacting many-body system [10, 12–14, 19, 32, 45–47]. The dynamics of a single probe spin generically depend on three properties: (i) the nature of the system-probe coupling [48], (ii) the system’s many-body Hamiltonian H_{int} , and (iii) the measurement sequence itself. Crucially, by averaging across the dynamics of many such probe spins, one can directly extract global features of the many-body system [Fig. 1(b)]. We distinguish between two types of ensemble averaging which give rise to distinct signatures in the decoherence: (i) an average over *many-body trajectories* (i.e. both spin configurations and dynamics) yields information about the microscopic spin fluctuations (for simplicity, we focus our discussion on the infinite-temperature limit [49]), (ii) an average over *positional randomness* (i.e. random locations of the system’s spins) yields information about both dimensionality and disorder.

To be specific, let us consider a single spin-1/2 probe coupled to a many-body ensemble via long-range, $1/r^\alpha$ Ising interactions:

$$H_z = \sum_i \frac{J_z}{r_i^\alpha} \hat{s}_p^z \hat{s}_i^z, \quad (1)$$

where r_i is the distance between the probe spin \hat{s}_p and the i -th system spin s_i [50]. Such power-law interactions are ubiquitous in solid-state, atomic and molecular quantum platforms (e.g. RKKY interactions, electric/magnetic dipolar interactions, van der Waals interactions, etc.) [6, 33, 42, 51].

Physically, the system spins generate an effective magnetic field at the location of the probe (via their Ising interactions), which can be measured via Ramsey spectroscopy [inset, Fig. 1(e)] [16]. In particular, we envision initially preparing the probe in an eigenstate of \hat{s}_p^z and subsequently rotating it with a $\pi/2$ -pulse such

that the normalized coherence, $C \equiv 2\langle \hat{s}_p^x \rangle = 1$. The magnetic field, which fluctuates due to many-body interactions, causes the probe to Larmor precess [inset, Fig. 1(b, e)] [52]. The phase associated with this Larmor precession can be read out via a population imbalance, after a second $\pi/2$ pulse.

Average over many-body trajectories—For a many-body system at infinite temperature, $C(t) = 2\text{Tr}[\rho(t)s_p^x]$, where $\rho(t)$ is the full density matrix that includes both the system and the probe [53]. Let us treat $\hat{s}_i^z(t) \rightarrow s_i^z(t)$ as a classical, stochastic random variable, whose dynamics are determined by H_{int} (e.g. coherent flip-flop interactions $\hat{s}_i^+ \hat{s}_j^-$). In this case, the phase of the aforementioned Larmor precession is given by $\phi(t) = \int_0^t dt' J_z \sum_i s_i^z(t')/r_i^\alpha$. Assuming that $\phi(t)$ is Gaussian-distributed, one finds that the average probe coherence decays exponentially as $C(t) = \langle e^{-i\phi(t)} \rangle = e^{-\langle \phi^2 \rangle / 2}$, where $\langle \phi^2 \rangle \sim \sum_i J_z^2 \chi(t)/r_i^{2\alpha}$ [5, 11, 19, 52, 54]. Here, $\chi(t)$ encodes the response of the probe spins to the noise spectral density, $S(\omega)$, of the many-body system:

$$\chi(t) \equiv \int d\omega |f(\omega; t)|^2 S(\omega), \quad (2)$$

where $f(\omega; t)$ is the filter function associated with a particular pulse sequence (e.g. Ramsey spectroscopy or spin echo) of total duration t [Fig. 1(e)] [55, 56].

Intuitively, $S(\omega)$ quantifies the noise power density of spin flips in the many-body system; it is the Fourier transform of the autocorrelation function, $\xi(t) \equiv 4\langle s_i^z(t)s_i^z(0) \rangle$, and captures the spin dynamics at the level of two-point correlations [57]. For Markovian dynamics, $\xi(t) = e^{-|t|/\tau_c}$, where τ_c defines the correlation time after which a spin, on average, retains no memory of its initial orientation [58]. In this case, $S(\omega)$ is Lorentzian and one can derive an analytic expression for χ [14, 32, 44, 45, 52, 56] [59].

A few remarks are in order. The premise that many-body Hamiltonian dynamics produce Gaussian-distributed phases $\phi(t)$ —while oft-assumed—is challenging to analytically justify [12, 14, 15, 60, 61]. Indeed, a

well-known counterexample of non-Gaussian spectral diffusion occurs when the spin dynamics can be modeled as telegraph noise – i.e. stochastic jumps between discrete values $s_i^z = \pm s_i$ [15, 62]; the precise physical settings where such noise emerges remains the subject of active debate [5, 12, 15, 44, 54, 56, 60, 62–67].

Average over positional randomness—The probe’s decoherence depends crucially on the spatial distribution of the spins in the many-body system. For disordered spins, explicitly averaging over their random positions yields a decoherence profile:

$$C(t) = \int \prod_{i=1}^N \frac{d^D r_i}{V} \exp \left[\frac{-J_z^2 \chi(t)}{2r_i^{2\alpha}} \right] = e^{-an[J_z^2 \chi(t)]^{D/2\alpha}}, \quad (3)$$

where a is a dimensionless constant, N is the number of system spins in a D -dimensional volume V at a density $n \equiv N/V$ [32, 52]. By contrast, for spins on a lattice or for a single probe spin, the exponent of the coherence scales as $\sim J_z^2 \chi(t)$ [52]. A particularly elegant intuition, based upon resonance-counting, underlies the appearance of both the dimensionality and the interaction power-law in Eqn. (3). Roughly, let us say that a probe spin is only coupled to system spins that induce a phase variance larger than some cutoff ϵ . This constraint on the minimum variance defines a volume of radius $r_{\max} \sim (J_z^2 \chi(t)/\epsilon)^{1/2\alpha}$ containing $N_s \sim nr_{\max}^D$ spins, implying that the total variance accrued at any given time is $\epsilon N_s \sim [J_z^2 \chi(t)]^{D/2\alpha}$. Thus, the positional average simply serves to count the number of spins to which the probe is coupled.

Decoherence profile—The functional form of the probe’s decoherence, $C(t)$, encodes a number of features of the many-body system. We begin by elucidating them in the context of Ramsey spectroscopy. First, one expects a somewhat sharp cross-over in the behavior of $C(t)$ at the correlation time τ_c . For early times, $t \ll \tau_c$, the phase variance accumulates as in a ballistic trajectory with $\chi \sim t^2$, while for late times, $t \gg \tau_c$, the variance accumulates as in a random walk with $\chi \sim t$ [10, 14, 45]. This leads to a simple prediction: namely, that the stretch-power, β , of the probe’s exponential decay (i.e. $-\log C(t) \sim t^\beta$) changes from D/α to $D/2\alpha$ at the correlation time [Fig. 1(f)].

Second, moving beyond Ramsey measurements by changing the filter function, one can probe even more subtle properties of the many-body noise. In particular, a spin-echo sequence filters out the leading order DC contribution from the many-body noise spectrum, allowing one to investigate higher-order correlation functions of the spin-flip dynamics. Different types of spin-flip dynamics naturally lead to different phase distributions. For the case of Gaussian noise, one finds that (at early times) $\chi \sim t^3$; however, in the case of telegraph noise the analysis is more subtle, since higher-order moments of $\phi(t)$ must be taken into account. This leads to markedly

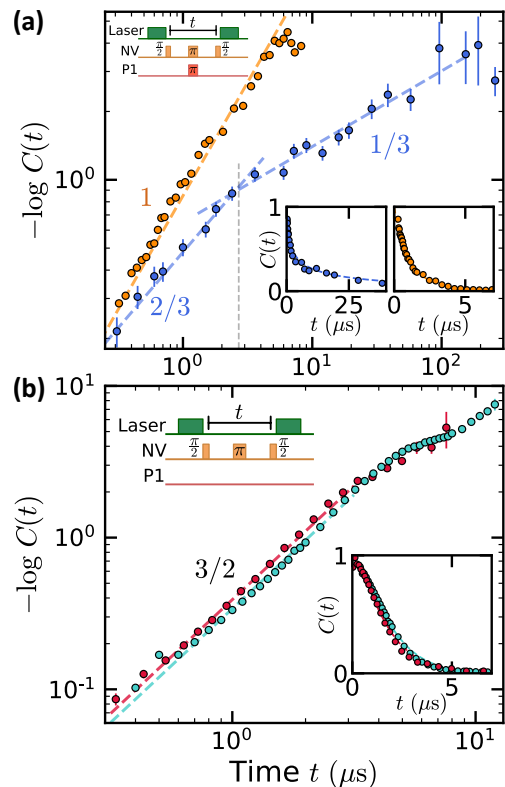


FIG. 2. (a) Depicts the normalized coherence for a DEER measurement on sample S1 (blue) and sample S2 (yellow) as a function of the free evolution time t . Dashed blue lines indicate the predicted early- and late-time stretch powers of $2/3$ and $1/3$, respectively, for a dipolar spin system in two dimensions. Dashed yellow line depicts the predicted early-time stretch power of 1 for a dipolar spin system in three dimensions [Table I]. Together, these data demonstrate the two- and three-dimensional nature of samples S1 and S2, respectively. Lower right insets show the same data on a linear scale. Top left inset shows the DEER pulse sequence. (b) Spin echo measurements on three-dimensional dipolar spin ensembles in samples S3 (teal) and S4 (pink) clearly exhibit a stretch power of $3/2$ (dotted lines) over nearly two decades in time. This is consistent with the presence of Gaussian noise and allows one to explicitly rule out telegraph noise. Lower right inset shows the same data on a linear scale. Top left inset shows the spin echo pulse sequence.

different early time predictions for β —dependent on both the measurement sequence as well as the many-body noise [Table I].

At late times, however, one expects the probe’s coherence to agree across different pulses sequences and spin-flip dynamics. For example, in the case of spin-echo, the decoupling π -pulse [inset, Fig. 1(e)] is ineffective on timescales larger than the correlation time, since the spin configurations during the two halves of the free evolution are completely uncorrelated. Moreover, this same loss of correlation implies that the phase accumulation is characterized by incoherent Gaussian diffusion regardless of the specific nature of the spin dynamics (e.g. Markovian

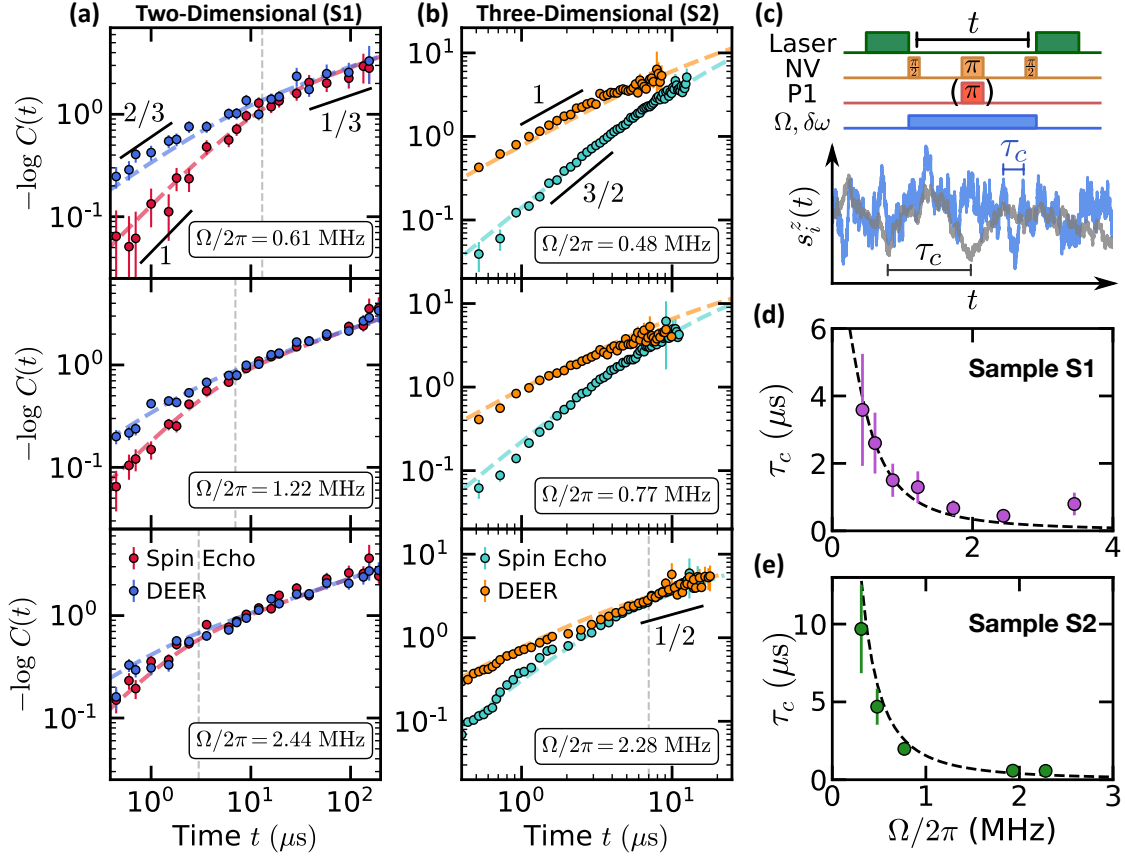


FIG. 3. (a,b) Measurements of DEER (blue, orange) and spin echo (red, teal) on two- and three-dimensional samples (S1, S2) for different powers of the polychromatic (i.e. incoherent) drive at fixed linewidth $\delta\omega = 2\pi \times (18, 20)$ MHz, respectively. The time at which the two signals overlap (vertical dashed lines) functions as a proxy for the correlation time and decreases as the power of the incoherent driving increases (top to bottom panels). The data is well-fit by analytic expressions for $\chi^{D/2\alpha}$ [Eqn. 5] (dashed curves). (c) An incoherent drive field (light blue) with power $\sim \Omega^2$ and linewidth $\delta\omega$ is applied to the P1 spins during the free evolution time t of both DEER and spin echo sequences in order to tune the correlation time of the many-body system. In this case, $s_i^z(t)$ evolves as a Gaussian random process. (d,e) The correlation times, τ_c , extracted from fitting the data to Eqn. 5 for samples S1 (purple) and S2 (green) are plotted as a function of Ω , and agree well with a simple theoretical model (dashed black curves) [52].

versus non-Markovian, or continuous versus telegraph).

Experimentally probing many-body noise in strongly-interacting spin ensembles

Our experimental samples contain a high density of spin-1/2 P1 centers [blue spins, Fig. 1(b)], which form a strongly-interacting many-body system coupled via magnetic dipole-dipole interactions:

$$H_{\text{int}} = \sum_{i < j} \frac{J_0}{r_{ij}^3} [c_{ij}(\hat{s}_i^+ \hat{s}_j^- + \hat{s}_i^- \hat{s}_j^+) + \tilde{c}_{ij} \hat{s}_i^z \hat{s}_j^z], \quad (4)$$

where $J_0 = 2\pi \times 52$ MHz·nm³, r_{ij} is the distance between P1 spins i and j , and c, \tilde{c} capture the angular dependence of the dipolar interaction [52]. We note that H_{int} contains only the energy-conserving terms of the dipolar interaction [68].

The probes in our system are spin-1 NV centers, which can be optically initialized to $|m_s = 0\rangle$ using 532 nm laser light. An applied magnetic field along the NV axis splits the $|m_s = \pm 1\rangle$ states, allowing us to work within the effective spin-1/2 manifold $\{|0\rangle, |-1\rangle\}$. Microwave pulses at frequency ω_{NV} are used to perform coherent spin rotations (i.e. for Ramsey spectroscopy or spin echo) within this manifold [Fig. 1(c)].

Physically, the NV and P1 centers are also coupled via dipolar interactions. However, for a generic magnetic field strength, they are highly detuned, i.e. $|\omega_{\text{NV}} - \omega_{\text{P1}}| \sim$ GHz, owing to the zero-field splitting of the NV center ($\Delta_0 = 2\pi \times 2.87$ GHz) [Fig. 1(c)]. Since typical interaction strengths in our system are on the order of \sim MHz, the direct polarization exchange between an NV and P1 is strongly off-resonant. This reduces the dipolar interaction between NV and P1 centers to a system-probe Ising coupling of precisely the form given by Eqn. 1 with

$\alpha = 3$ [52].

Delta-doped sample fabrication—Sample S1 was grown via homoepitaxial plasma-enhanced chemical vapor deposition (PECVD) using isotopically purified methane (99.999% ^{12}C) [39]. The delta-doped layer was formed by introducing natural-abundance nitrogen gas during growth (5 sccm, 10 minutes) in between nitrogen-free buffer and capping layers. To create the vacancies necessary for generating NV centers, the sample was electron-irradiated with a transmission electron microscope set to 145 keV [40] and subsequently annealed at 850° C for 6 hours.

Two-dimensional spin dynamics—We begin by performing double electron-electron resonance (DEER) measurements on sample S1. While largely analogous to Ramsey spectroscopy [Table I] [69], DEER has the technical advantage that it filters out undesired quasi-static fields (e.g. from hyperfine interactions between the NV and host nitrogen nucleus) [16, 41, 70]. As shown in Fig. 2(a) [blue data, inset], the NV’s coherence decays on a time scale $\sim 5 \mu\text{s}$.

To explore the functional form of the probe NV’s decoherence, we plot the negative logarithm of the coherence, $-\log C(t)$, on a log-log scale, such that the stretch power, β , is simply given by the slope of the data. At early times, the data exhibit $\beta = 2/3$ for over a decade in time [blue data, Fig. 2(a)]. At a timescale $\sim 3 \mu\text{s}$ (vertical dashed line), the data crosses over to a stretch power of $\beta = 1/3$ for another decade in time. This behavior is in excellent agreement with that expected for two-dimensional spin dynamics driven by dipolar interactions [Fig. 1(f), Table I].

Finally, for comparison, we perform DEER spectroscopy on a conventional three-dimensional NV-P1 system (sample S2, see Methods). As shown in Fig. 2(a) (orange), the data exhibit $\beta = 1$ for a decade in time, consistent with the prediction for three-dimensional dipolar interactions [Table I]. However, the crossover to the late-time “random walk” regime is difficult to experimentally access because the larger early-time stretch power causes a faster decay to the noise floor.

Characterizing microscopic spin-flip dynamics—To probe the nature of the microscopic spin-flip dynamics in our system, we perform spin-echo measurements on three dimensional samples [S3, S4 (Type IB)], which exhibit a significantly higher P1-to-NV density ratio (see Methods). For lower relative densities (i.e. samples S1 and S2), the spin echo measurement contains a confounding signal from interactions between the NVs themselves (see Methods).

In both samples (S3, S4), we find that the coherence exhibits a stretched exponential decay with $\beta = 3/2$ for well over a decade in time [Fig. 2(b)]. Curiously, this is consistent with Gaussian spectral diffusion where $\beta = 3D/2\alpha = 3/2$ and patently inconsistent with the telegraph noise prediction of $\beta = 1 + D/\alpha = 2$. While in

agreement with prior measurements on similar samples [67], this observation is actually rather puzzling and related to an enduring question in the context of dipolar spin noise [10–16, 32, 42].

In particular, one naively expects that spins in a strongly-interacting system should be treated as stochastic binary variables, thereby generating telegraph noise; for the specific case of dipolar spin ensembles, this expectation dates back to seminal work from Klauder and Anderson [12]. The intuition behind this is perhaps most easily seen in the language of the master equation—each individual spin sees the remaining system as a Markovian bath. The resulting local spin dynamics is then characterized by a series of stochastic quantum jumps, giving rise to telegraph noise [52]. Alternatively, in the Heisenberg picture, the same intuition can be understood from the spreading of the operator \hat{s}_i^z ; this spreading hides local coherences in many-body correlations, leading to an ensemble of telegraph-like, classical trajectories [52].

We conjecture that the origin of Gaussian spectral diffusion in our system is related to the presence of disorder, which strongly suppresses operator spreading [71]. To illustrate this point, consider the limiting case where the operator dynamics are constrained to a single spin. In this situation, the dynamics of $\hat{s}_i^z(t)$ follows a particular coherent trajectory around the Bloch sphere, and the rate at which the probe accumulates phase is continuous [52]. Averaging over different trajectories of the coherent dynamics naturally leads to Gaussian noise [52].

Controlling the many-body spectral function—Finally, we demonstrate the ability to directly control the many-body noise spectrum for both two- and three-dimensional dipolar spin ensembles (i.e. samples S1, S2). In particular, we engineer the shape and linewidth of $S(\omega)$ by driving the P1 system with a polychromatic microwave tone [43]. This drive is generated by adding phase noise to the resonant microwave signal at ω_{P1} in order to produce a Lorentzian drive spectrum with linewidth $\delta\omega$ [Fig. 3(c)].

Microscopically, the polychromatic drive leads to a number of physical effects. First, tuning the Rabi frequency, Ω , of the drive provides a direct knob for controlling the correlation time, τ_c , of the P1 system. Second, since the many-body system inherits the noise spectrum of the drive, one has provably Gaussian statistics for the spin variables s_i^z [52]. Third, our earlier Markovian assumption is explicitly enforced by the presence of a Lorentzian noise spectrum. Taking these last two points together allows one to analytically predict the precise form of the NV probe’s decoherence profile, $-\log C(t) \sim \chi(t)^{D/2\alpha}$, for either DEER or spin-echo spectroscopy:

$$\begin{aligned}\chi^{\text{DEER}}(t) &= 2\tau_c t - 2\tau_c^2(1 - e^{-\frac{t}{\tau_c}}), \\ \chi^{\text{SE}}(t) &= 2\tau_c t - 2\tau_c^2(3 + e^{-\frac{t}{\tau_c}} - 4e^{-\frac{t}{2\tau_c}}).\end{aligned}\tag{5}$$

We perform both DEER and spin-echo measurements as a function of the power ($\sim \Omega^2$) of the polychromatic drive for our two-dimensional sample (S1) [Fig. 3(a)]. As expected, for weak driving [top, Fig. 3(a)], the DEER signal (blue) is analogous to the undriven case, exhibiting a cross-over from a stretch power of $\beta = 2/3$ at early times to a stretch power of $\beta = 1/3$ at late times. For the same drive strength, the spin echo data (red) also exhibits a cross over between two distinct stretch powers, with the key difference being that $\beta = 3D/2\alpha = 1$ at early times. This represents an independent (spin-echo-based) confirmation of the two-dimensional nature of our delta-doped sample.

Recall that at late times (i.e. $t \gtrsim \tau_c$), one expects the NV's coherence $C(t)$ to agree across different pulses sequences [Fig. 1(f)]. This is indeed borne out by the data [Fig. 3]. In fact, the location of this late-time overlap provides a proxy for estimating the correlation time and is shown as the dashed grey lines in Fig. 3(a). As one increases the power of the drive [Fig. 3(a)], the noise spectrum, $S(\omega)$, naturally broadens. In the data, this manifests as a shortened correlation time, with the location of the DEER/echo overlap shifting to earlier time-scales [Fig. 3(a)].

Analogous measurements on a three dimensional spin ensemble (sample S2), reveal much the same physics [Fig. 3(b)], with stretch powers again consistent with a Gauss-Markov prediction [Table I]. For weak driving, $C(t)$ is consistent with the early-time ballistic regime for over a decade in time [Fig. 3b, top panel]; however, it is difficult to access late enough time-scales to observe an overlap between DEER and spin echo. Crucially, by using the drive to push to shorter correlation times, we can directly observe the late-time random-walk regime in three dimensions, where $\beta = 1/2$ [Fig. 3b, bottom panel].

Remarkably, as evidenced by the dashed curves in Fig. 3(a,b), our data exhibits excellent agreement—across different dimensionalities, drive strengths, and pulse sequences—with the analytic predictions presented in Eqn. 5. Moreover, by fitting $\chi^{D/2\alpha}$ simultaneously across spin echo and DEER datasets for each Ω , we quantitatively extract the correlation time, τ_c . Up to an $\mathcal{O}(1)$ scaling factor, we find that the extracted τ_c agrees well with the DEER/echo overlap time. In addition, the behavior of τ_c as a function of Ω , also exhibits quantitative agreement with an analytic model that predicts $\tau_c \sim \delta\omega/\Omega^2$ in the limit of strong driving [Fig. 3(d,e)] [52].

Finally, we emphasize that although one observes $\beta = 3D/2\alpha$ in both the driven [Fig. 3(a,b)] and undriven [Fig. 2(b)] spin echo measurements, the underlying physics is extremely different. In the latter case, Gaussian spectral diffusion emerges from isolated, disordered, many-body dynamics, while in the former case, it is imposed by the external drive.

Conclusion and Outlook

Our results demonstrate the diversity of information that can be accessed via the decoherence dynamics of a probe spin ensemble. For example, we shed light on a long-standing debate about the nature of spin-flip noise in a strongly-interacting dipolar system [5, 12, 15, 44, 54, 56, 60, 62–67]. Moreover, we directly measure the correlation time of the many-body system and introduce a technique to probe its dimensionality. This technique is particularly useful for spin ensembles embedded in solids [72–74], where a direct, non-destructive measurement of nanoscale spatial properties is challenging with conventional toolsets.

One can imagine generalizing our work in a number of promising directions. First, the ability to fabricate and characterize strongly-interacting, two-dimensional dipolar spin ensembles opens the door to a number of intriguing questions within the landscape of quantum simulation. Indeed, dipolar interactions in 2D are quite special from the perspective of localization, allowing one to experimentally probe the role of many-body resonances [75–77]. In the context of ground state physics, the long-range, anisotropic nature of the dipolar interaction has also been predicted to stabilize a number of exotic phases, ranging from supersolids to spin liquids [78–80]. Connecting this latter point back to noise spectroscopy, one could imagine tailoring the probe's filter function to distinguish between different types of ground-state order [22, 23].

Second, dense ensembles of two dimensional spins also promise a number of unique advantages with respect to quantum sensing [39, 41, 81, 82]. For example, a 2D layer of NVs fabricated near the diamond surface would exhibit a significant enhancement in spatial resolution (set by the depth of the layer) compared to a three-dimensional ensemble at the same density, ρ [39, 83, 84]. In addition, for samples where the coherence time is limited by spin-spin interactions, a lower dimensionality reduces the coordination number and leads to an enhanced T_2 scaling as $\rho^{-\alpha/D}$ [85].

Third, one can probe the relationship between operator spreading and Gauss-Markov noise by exploring samples with different relaxation rates, interaction power-laws, disorder strengths and spin densities [44, 60]. One could also utilize alternate pulse sequences, such as stimulated echo, to provide a more fine-grained characterization of the many-body noise (e.g. the entire spectral diffusion kernel) [10, 60, 86].

Finally, our framework can also be applied to long-range-interacting systems of Rydberg atoms, trapped ions, and polar molecules [33–38]. In such systems, the ability to perform imaging and quantum control at the single-particle level allows for greater freedom in designing methods to probe many-body noise. As a particularly

intriguing example, one could imagine a non-destructive, time-resolved generalization of many-body noise spectroscopy, where one repeatedly interrogates the probe without projecting the many-body system.

Note added: During the completion of this work, we became aware of complementary work using single NV centers to measure the noise from a 2D disordered spin ensemble on the diamond surface [87], which will appear in the same arXiv posting. Both works use the decoherence profile of the probe spin to characterize the dimensionality and dynamics of the many-body system.

Acknowledgments: We gratefully acknowledge the insights of and discussions with M. Aidelsburger, D. Awschalom, B. Dwyer, C. Laumann, J. Moore, E. Urbach, and H. Zhou. This work was supported by the Center for Novel Pathways to Quantum Coherence in Materials, an Energy Frontier Research Center funded by the U.S. Department of Energy, Office of Science, Basic Energy Sciences (materials growth, sample characterization, and noise spectroscopy), the US Department of Energy (BES grant No. DE-SC0019241) for driving studies, and the Army Research Office through the MURI program (grant number W911NF-20-1-0136) for theoretical studies, the W. M. Keck foundation, the David and Lucile Packard foundation, and the A. P. Sloan foundation. E.J.D. acknowledges support from the Miller Institute for Basic Research in Science. S.A.M. acknowledges the support of the Natural Sciences and Engineering Research Council of Canada (NSERC), (funding reference number AID 516704-2018) and the NSF Quantum Foundry through Q-AMASE-i program award DMR-1906325. D.B. acknowledges support from the NSF Graduate Research Fellowship Program (grant DGE1745303) and The Fannie and John Hertz Foundation.

* Equal contribution

† ania@physics.ucsb.edu

‡ norman.yao@berkeley.edu

- [1] Purcell, E. M. Spontaneous emission probabilities at radio frequencies. In *Confined Electrons and Photons*, 839–839 (Springer, 1995).
- [2] Kleppner, D. Inhibited spontaneous emission. *Physical review letters* **47**, 233 (1981).
- [3] Viola, L., Knill, E. & Lloyd, S. Dynamical decoupling of open quantum systems. *Phys. Rev. Lett.* **82**, 2417–2421 (1999). URL <https://link.aps.org/doi/10.1103/PhysRevLett.82.2417>.
- [4] Houck, A. *et al.* Controlling the spontaneous emission of a superconducting transmon qubit. *Physical review letters* **101**, 080502 (2008).
- [5] De Lange, G., Wang, Z., Riste, D., Dobrovitski, V. & Hanson, R. Universal dynamical decoupling of a single solid-state spin from a spin bath. *Science* **330**, 60–63 (2010).
- [6] Saffman, M., Walker, T. G. & Mølmer, K. Quantum information with rydberg atoms. *Rev. Mod. Phys.* **82**, 2313–2363 (2010). URL <https://link.aps.org/doi/10.1103/RevModPhys.82.2313>.
- [7] Bylander, J. *et al.* Noise spectroscopy through dynamical decoupling with a superconducting flux qubit. *Nature Physics* **7**, 565–570 (2011).
- [8] Kim, Z. *et al.* Decoupling a cooper-pair box to enhance the lifetime to 0.2 ms. *Physical review letters* **106**, 120501 (2011).
- [9] Tyryshkin, A. M. *et al.* Electron spin coherence exceeding seconds in high-purity silicon. *Nature materials* **11**, 143–147 (2012).
- [10] Anderson, P. W. & Weiss, P. R. Exchange narrowing in paramagnetic resonance. *Rev. Mod. Phys.* **25**, 269–276 (1953). URL <https://link.aps.org/doi/10.1103/RevModPhys.25.269>.
- [11] Herzog, B. & Hahn, E. L. Transient nuclear induction and double nuclear resonance in solids. *Phys. Rev.* **103**, 148–166 (1956). URL <https://link.aps.org/doi/10.1103/PhysRev.103.148>.
- [12] Klauder, J. & Anderson, P. Spectral diffusion decay in spin resonance experiments. *Physical Review* **125**, 912 (1962).
- [13] Kubo, R., Toda, M. & Hashitsume, N. *Statistical physics II: nonequilibrium statistical mechanics*, vol. 31 (Springer Science & Business Media, 2012).
- [14] Salikhov, K., Dzuba, S.-A. & Raitsimring, A. M. The theory of electron spin-echo signal decay resulting from dipole-dipole interactions between paramagnetic centers in solids. *Journal of Magnetic Resonance (1969)* **42**, 255–276 (1981).
- [15] Chiba, M. & Hirai, A. Electron spin echo decay behaviours of phosphorus doped silicon. *Journal of the Physical Society of Japan* **33**, 730–738 (1972).
- [16] Schweiger, A. & Jeschke, G. *Principles of pulse electron paramagnetic resonance* (Oxford University Press on Demand, 2001).
- [17] Mittiga, T. *et al.* Imaging the local charge environment of nitrogen-vacancy centers in diamond. *Physical review letters* **121**, 246402 (2018).
- [18] Hsieh, S. *et al.* Imaging stress and magnetism at high pressures using a nanoscale quantum sensor. *Science* **366**, 1349–1354 (2019).
- [19] Wang, Z.-H., De Lange, G., Ristè, D., Hanson, R. & Dobrovitski, V. Comparison of dynamical decoupling protocols for a nitrogen-vacancy center in diamond. *Physical Review B* **85**, 155204 (2012).
- [20] Altman, E., Demler, E. & Lukin, M. D. Probing many-body states of ultracold atoms via noise correlations. *Physical Review A* **70**, 013603 (2004).
- [21] Hofferberth, S. *et al.* Probing quantum and thermal noise in an interacting many-body system. *Nature Physics* **4**, 489–495 (2008).
- [22] Chatterjee, S., Rodriguez-Nieva, J. F. & Demler, E. Diagnosing phases of magnetic insulators via noise magnetometry with spin qubits. *Physical Review B* **99**, 104425 (2019).
- [23] Khoo, J. Y., Pientka, F. & Sodemann, I. The universal shear conductivity of fermi liquids and spinon fermi surface states and its detection via spin qubit noise magnetometry. *arXiv preprint arXiv:2103.05095* (2021).
- [24] Paris, M. & Rehacek, J. *Quantum state estimation*, vol. 649 (Springer Science & Business Media, 2004).
- [25] Häffner, H. *et al.* Scalable multiparticle entanglement of trapped ions. *Nature* **438**, 643–646 (2005).

- [26] Mertens, C., Kennedy, T. & Swain, S. Many-body theory of quantum noise. *Physical review letters* **71**, 2014 (1993).
- [27] Cherng, R. W. & Demler, E. Quantum noise analysis of spin systems realized with cold atoms. *New Journal of Physics* **9**, 7 (2007).
- [28] Faoro, L. & Ioffe, L. B. Microscopic origin of low-frequency flux noise in josephson circuits. *Physical review letters* **100**, 227005 (2008).
- [29] Bruun, G., Andersen, B. M., Demler, E. & Sørensen, A. S. Probing spatial spin correlations of ultracold gases by quantum noise spectroscopy. *Physical review letters* **102**, 030401 (2009).
- [30] Roy, D., Singh, R. & Moessner, R. Probing many-body localization by spin noise spectroscopy. *Physical Review B* **92**, 180205 (2015).
- [31] Hetterich, D., Yao, N. Y., Serbyn, M., Pollmann, F. & Trauzettel, B. Detection and characterization of many-body localization in central spin models. *Physical Review B* **98**, 161122 (2018).
- [32] Fel'dman, E. B. & Lacelle, S. Configurational averaging of dipolar interactions in magnetically diluted spin networks. *The Journal of chemical physics* **104**, 2000–2009 (1996).
- [33] Britton, J. W. *et al.* Engineered two-dimensional ising interactions in a trapped-ion quantum simulator with hundreds of spins. *Nature* **484**, 489–492 (2012).
- [34] Joshi, M. K. *et al.* Quantum information scrambling in a trapped-ion quantum simulator with tunable range interactions. *Phys. Rev. Lett.* **124**, 240505 (2020). URL <https://link.aps.org/doi/10.1103/PhysRevLett.124.240505>.
- [35] Zeiher, J. *et al.* Many-body interferometry of a rydberg-dressed spin lattice. *Nature Physics* **12**, 1095–1099 (2016).
- [36] Zeiher, J. *et al.* Coherent many-body spin dynamics in a long-range interacting ising chain. *Phys. Rev. X* **7**, 041063 (2017). URL <https://link.aps.org/doi/10.1103/PhysRevX.7.041063>.
- [37] Borish, V., Marković, O., Hines, J. A., Rajagopal, S. V. & Schleier-Smith, M. Transverse-field ising dynamics in a rydberg-dressed atomic gas. *Physical review letters* **124**, 063601 (2020).
- [38] Ni, K.-K. *et al.* A high phase-space-density gas of polar molecules. *science* **322**, 231–235 (2008).
- [39] Ohno, K. *et al.* Engineering shallow spins in diamond with nitrogen delta-doping. *Applied Physics Letters* **101**, 082413 (2012).
- [40] McLellan, C. A. *et al.* Patterned formation of highly coherent nitrogen-vacancy centers using a focused electron irradiation technique. *Nano letters* **16**, 2450–2454 (2016).
- [41] Eichhorn, T. R., McLellan, C. A. & Bleszynski Jayich, A. C. Optimizing the formation of depth-confined nitrogen vacancy center spin ensembles in diamond for quantum sensing. *Phys. Rev. Materials* **3**, 113802 (2019). URL <https://link.aps.org/doi/10.1103/PhysRevMaterials.3.113802>.
- [42] Choi, J. *et al.* Depolarization dynamics in a strongly interacting solid-state spin ensemble. *Phys. Rev. Lett.* **118**, 093601 (2017). URL <https://link.aps.org/doi/10.1103/PhysRevLett.118.093601>.
- [43] Joos, M., Bluvstein, D., Lyu, Y., Weld, D. M. & Jayich, A. B. Protecting qubit coherence by spectrally engineered driving of the spin environment (2021). 2101.09654.
- [44] Glasbeek, M. & Hond, R. Phase relaxation of photoexcited triplet spins in cao. *Physical Review B* **23**, 4220 (1981).
- [45] Hu, P. & Hartmann, S. R. Theory of spectral diffusion decay using an uncorrelated-sudden-jump model. *Phys. Rev. B* **9**, 1–13 (1974). URL <https://link.aps.org/doi/10.1103/PhysRevB.9.1>.
- [46] Cucchietti, F. M., Paz, J. P. & Zurek, W. H. Decoherence from spin environments. *Phys. Rev. A* **72**, 052113 (2005). URL <https://link.aps.org/doi/10.1103/PhysRevA.72.052113>.
- [47] de Sousa, R. Electron spin as a spectrometer of nuclear-spin noise and other fluctuations. *Electron Spin Resonance and Related Phenomena in Low-Dimensional Structures* 183–220 (2009). URL http://dx.doi.org/10.1007/978-3-540-79365-6_10.
- [48] Although we have been explicitly distinguishing between the probe and the system, we note that our framework also applies to the scenario where the probe itself is a part of the many-body system.
- [49] The analysis is easily extended to finite temperature, but subtleties arise for low-temperature ordered states.
- [50] The Ising coupling J_z implicitly includes any angular dependence of e.g. dipolar interactions.
- [51] Craig, N. J. *et al.* Tunable Nonlocal Spin Control in a Coupled-Quantum Dot System. *Science* **304**, 565–567 (2004).
- [52] See Supplemental Information at [URL will be inserted by publisher] for supporting derivations, including Refs. XXX.
- [53] The full density matrix $\rho(t)$ includes both the system and the probe, and is time-evolved under the system interactions H_{int} , the probe-system coupling H_z , and the measurement pulse sequence.
- [54] Hanson, R., Dobrovitski, V., Feiguin, A., Gywat, O. & Awschalom, D. Coherent dynamics of a single spin interacting with an adjustable spin bath. *Science* **320**, 352–355 (2008).
- [55] Cywiński, L., Lutchyn, R. M., Nave, C. P. & Das Sarma, S. How to enhance dephasing time in superconducting qubits. *Phys. Rev. B* **77**, 174509 (2008). URL <https://link.aps.org/doi/10.1103/PhysRevB.77.174509>.
- [56] Wang, Z.-H. & Takahashi, S. Spin decoherence and electron spin bath noise of a nitrogen-vacancy center in diamond. *Physical Review B* **87**, 115122 (2013).
- [57] Kogan, S. *Electronic noise and fluctuations in solids* (Cambridge University Press, 2008).
- [58] Note that the Markovian assumption is not necessarily valid for a many-body system at early times or for certain forms of interactions [47].
- [59] In general, χ can be computed numerically for an arbitrary spectral function $S(\omega)$.
- [60] Mims, W. Phase memory in electron spin echoes, lattice relaxation effects in caw o 4: Er, ce, mn. *Physical Review* **168**, 370 (1968).
- [61] Witzel, W. & Sarma, S. D. Quantum theory for electron spin decoherence induced by nuclear spin dynamics in semiconductor quantum computer architectures: Spectral diffusion of localized electron spins in the nuclear solid-state environment. *Physical Review B* **74**, 035322 (2006).
- [62] Abe, E., Itoh, K. M., Isoya, J. & Yamasaki, S. Electron-spin phase relaxation of phosphorus donors in nuclear-spin-enriched silicon. *Physical Review B* **70**, 033204

- (2004).
- [63] Zhidomirov, G. & Salikhov, K. Contribution to the theory of spectral diffusion in magnetically diluted solids. *Soviet Journal of Experimental and Theoretical Physics* **29**, 1037 (1969).
- [64] Zhong, M. *et al.* Optically addressable nuclear spins in a solid with a six-hour coherence time. *Nature* **517**, 177–180 (2015).
- [65] de Sousa, R. & Sarma, S. D. Theory of nuclear-induced spectral diffusion: Spin decoherence of phosphorus donors in si and gaas quantum dots. *Physical Review B* **68**, 115322 (2003).
- [66] Witzel, W., de Sousa, R. & Sarma, S. D. Quantum theory of spectral-diffusion-induced electron spin decoherence. *Physical Review B* **72**, 161306 (2005).
- [67] Bauch, E. *et al.* Decoherence of ensembles of nitrogen-vacancy centers in diamond. *Phys. Rev. B* **102**, 134210 (2020). URL <https://link.aps.org/doi/10.1103/PhysRevB.102.134210>.
- [68] Zu, C., Machado, F., Ye, B. *et al.* Emergent hydrodynamics in a strongly interacting dipolar spin ensemble. *under review* (2021).
- [69] We note that this is the case for dense P1 ensembles where the NV's Ramsey signal is dominated by the P1 bath.
- [70] De Lange, G. *et al.* Controlling the quantum dynamics of a mesoscopic spin bath in diamond. *Scientific reports* **2**, 1–5 (2012).
- [71] Witzel, W. M., Carroll, M. S., Cywiński, L. & Sarma, S. D. Quantum decoherence of the central spin in a sparse system of dipolar coupled spins. *Physical Review B* **86**, 035452 (2012).
- [72] Cappellaro, P., Ramanathan, C. & Cory, D. G. Dynamics and control of a quasi-one-dimensional spin system. *Phys. Rev. A* **76**, 032317 (2007). URL <https://link.aps.org/doi/10.1103/PhysRevA.76.032317>.
- [73] Lukin, D. M., Guidry, M. A. & Vučković, J. Integrated quantum photonics with silicon carbide: Challenges and prospects. *PRX Quantum* **1**, 020102 (2020). URL <https://link.aps.org/doi/10.1103/PRXQuantum.1.020102>.
- [74] Gangloff, D. A. *et al.* Revealing beyond-mean-field correlations in a nuclear ensemble via a proxy qubit. *arXiv preprint arXiv:2012.11279* (2020).
- [75] Burin, A. L. Many-Body Delocalization in Strongly Disordered System with Long-Range Interactions: Finite Size Scaling. *arXiv:1409.7990 [cond-mat, physics:quant-ph]* (2015). 1409.7990.
- [76] Yao, N. Y. *et al.* Many-body Localization with Dipoles. *Physical Review Letters* **113**, 243002 (2014). 1311.7151.
- [77] Safavi-Naini, A., Wall, M. L., Acevedo, O. L., Rey, A. M. & Nandkishore, R. M. Quantum dynamics of disordered spin chains with power-law interactions. *Physical Review A* **99**, 033610 (2019).
- [78] Yao, N. Y., Zaletel, M. P., Stamper-Kurn, D. M. & Vishwanath, A. A quantum dipolar spin liquid. *Nature Physics* **14**, 405–410 (2018).
- [79] Zou, H., Zhao, E. & Liu, W. V. Frustrated magnetism of dipolar molecules on a square optical lattice: Prediction of a quantum paramagnetic ground state. *Physical review letters* **119**, 050401 (2017).
- [80] Chomaz, L. *et al.* Long-lived and transient supersolid behaviors in dipolar quantum gases. *Physical Review X* **9**, 021012 (2019).
- [81] Sushkov, A. *et al.* Magnetic resonance detection of individual proton spins using quantum reporters. *Physical review letters* **113**, 197601 (2014).
- [82] Choi, S., Yao, N. Y. & Lukin, M. D. Quantum metrology based on strongly correlated matter. *arXiv preprint arXiv:1801.00042* (2017).
- [83] Roskopf, T. *et al.* Investigation of surface magnetic noise by shallow spins in diamond. *Physical review letters* **112**, 147602 (2014).
- [84] Pham, L. M. *et al.* Nmr technique for determining the depth of shallow nitrogen-vacancy centers in diamond. *Physical Review B* **93**, 045425 (2016).
- [85] While there exist surface spins on diamond which are also naturally confined to two dimensions, these spins exhibit significantly shorter coherence times compared to NV/P1 centers within the diamond lattice [81].
- [86] Van Oort, E. & Glasbeek, M. Optically detected low field electron spin echo envelope modulations of fluorescent nv centers in diamond. *Chemical physics* **143**, 131–140 (1990).
- [87] Dwyer, B. L. *et al.* Probing spin dynamics on diamond surfaces using a single quantum sensor. *Manuscript in preparation* .

Methods and Extended Data: Probing many-body noise in a strongly-interacting two-dimensional dipolar spin system

Emily J. Davis,^{1,*} Bingtian Ye,^{1,*} Francisco Machado,^{1,2,*} Simon A. Meynell,³ Thomas Mittiga,^{1,2} William Schenken,³ Maxime Joos,³ Bryce Kobrin,^{1,2} Yuanqi Lyu,¹ Dolev Bluvstein,⁴ Soonwon Choi,¹ Chong Zu,^{1,2,5} Ania C. Bleszynski Jayich,^{3,†} and Norman Y. Yao^{1,2,‡}

¹*Department of Physics, University of California, Berkeley, CA 94720, USA*

²*Materials Science Division, Lawrence Berkeley National Laboratory, Berkeley, CA 94720, USA*

³*Department of Physics, University of California, Santa Barbara, CA 93106, USA*

⁴*Department of Physics, Harvard University, Cambridge, MA 02138, USA*

⁵*Department of Physics, Washington University, St. Louis, MO 63130, USA*

I. SAMPLE S1

I.1. Sample Fabrication

We here provide further details on sample S1, which was grown on a commercially-available Element-6 electronic grade (100) substrate, polished by Syntek [1] to a surface roughness less than 200 pm. Throughout the PECVD growth process [2], we used 400 sccm of hydrogen gas with a background pressure of 25 Torr, and a microwave power of 750 W. The sample temperature was held at 800°C.

I.2. NV Density Estimation

We estimate the NV areal density in sample S1 via the measured NV decoherence for an XY-8 pulse sequence [inset, Fig. E1(a)] [3]. In this measurement, the NV decoherence is dominated by NV-NV interactions. In particular, decoherence caused by P1 spin-flip noise is largely suppressed due to our choice of interpulse spacing $\tau_p = 500$ ns, which is much shorter than the correlation time τ_c of the P1 system. As a result, the XY-8 data corresponds to a Ramsey measurement of the NV-NV interactions within the NV group aligned with the applied magnetic field B . These NV centers, representing 1/4 of the total number of NVs, all have the same microwave transition frequency and thus cannot be trivially decoupled from each other. For a known dipolar coupling strength $J_0 = 2\pi \times 52$ MHz·nm³, the average three-dimensional NV density n_{3D}^{NV} (with units $[n_{3D}^{NV}] = \text{nm}^{-3}$, and not to be confused with the D -dimensional density n defined in the main text) fixes an average interaction strength from which the decay timescale can be calculated. Here, we approximate the decoherence of the NV centers as arising solely from the Ising interactions between them, which is reasonable at least at short times when the NVs are spin-polarized.

We compare the XY-8 measurement with a numerically-computed Ramsey signal, which is generated as follows: we consider a central probe NV interacting with a bath of other NVs, placed randomly in a thin slab of thickness w and density $n_{3D}^{NV}/4$ (corresponding to the NV group that is addressed by our pulse sequence). After selecting a random spin configuration for the bath NVs, we compute the Ramsey signal $\sim \cos(\phi)$ for the probe NV. We then average over many such samples. The resulting curve corresponds to an average of the coherent NV oscillations over the positional and configurational realizations of the bath NVs, and exhibits a stretched exponential decay of the form $C(t) = e^{-(t/T_2^*)^{2/3}}$. We note that this matches our expectation for the early-time ballistic regime [Table 1 in the main text], because we have not included any flip-flop dynamics in the numerical model.

With the above prescription, we produce a set of numerically-computed Ramsey signals [dashed lines, Fig. E1(a)] as a function of areal density $n_{3D}^{NV} \cdot w$, which we compare against the XY-8 data [orange points, Fig. E1(a)]. The numerical curves plotted in Fig. E1(a) are independent of the thickness w , for w smaller than the upper bound of $w = 8$ nm obtained from the SIMS measurement [Fig. 1(d) in the main text]; the resulting decoherence only depends on the areal density $n_{3D}^{NV} \cdot w$ of sample S1. The estimated areal density is thus $n_{3D}^{NV} \cdot w = 12 \pm 2$ ppm · nm $\sim 0.0021(4)$ nm⁻², corresponding to a density of $n_{3D}^{NV} = 1.5 \pm 0.3$ ppm assuming a $w = 8$ nm-thick 2D layer. At late times, the XY-8

* Equal contribution

† ania@physics.ucsb.edu

‡ norman.yao@berkeley.edu

data begins to curve downwards (grey shaded area), as the measurement starts to access the late-time “random-walk” regime. This behavior is caused by spin-flips in the bath of NVs, which are not captured by the pure Ising interactions in the numerical model; we thus do not include this portion of the measurement in the density estimation.

I.3. P1 Density Estimation

Estimation of the P1 density is analogous to the previous discussion, with the simple substitution of a DEER measurement sequence for XY-8. We first subtract the contribution due to NV-NV interactions from the DEER signal; explicitly, we subtract an interpolation of the XY-8 data plotted in Fig. E1(a) from the raw DEER data. Then, we compare the numerically-computed decoherence for a density $n_{3D}^{P1}/3$ of P1s with the observed early time dynamics, as shown in Fig. E1(b). Here, we include a factor of 1/3 in the P1 density because our microwave tone ω_{P1} addresses only one-third of all the P1 spins in our DEER measurement; these spins are spectroscopically separated from the others due to the hyperfine interaction between the P1 electronic and nuclear spins [4, 5]. The estimated areal density is then $n_{3D}^{P1} \cdot w = 64 \pm 8 \text{ ppm} \cdot \text{nm} \sim 0.011(1) \text{ nm}^{-2}$, corresponding to a density of $n_{3D}^{P1} = 8 \pm 1 \text{ ppm}$ assuming a $w = 8 \text{ nm}$ -thick 2D layer. We again ignore the late-time $t \gg \tau_c$ region (gray shaded area) when comparing the measurement to the numerical curves.

II. SAMPLE S2

A detailed characterization of the three-dimensional sample S2 is given in Ref. [6] (sample C041). Here, we describe the key properties relevant for the present study. The sample was grown by depositing a 32 nm diamond buffer layer, followed by a 500 nm nitrogen-doped layer (99% ^{15}N), and finished with a 50 nm undoped diamond capping layer. Vacancies were created by irradiating with 145 keV electrons at a dosage of 10^{21} cm^{-2} , and vacancy diffusion was activated by annealing at 850°C for 48 hours in an Ar/Cl atmosphere. The resulting NV density is $\sim 0.4 \text{ ppm}$, obtained through instantaneous diffusion measurements [6]. The P1 density is measured to be $\sim 20 \text{ ppm}$ through a modified DEER sequence [6]. The average spacing between P1 centers ($\sim 4 \text{ nm}$) is much smaller than the thickness of the nitrogen doped layer, ensuring three-dimensional behavior of the spin ensemble.

III. SAMPLES S3 AND S4

Samples S3 and S4 used in this work are synthetic type-Ib single crystal diamonds (Element Six) with intrinsic substitutional ^{14}N concentration $\sim 100 \text{ ppm}$ (calibrated with an NV linewidth measurement [5]). To create NV centers, the samples were first irradiated with electrons (2 MeV energy and $1 \times 10^{18} \text{ cm}^{-2}$ dosage) to generate vacancies. After irradiation, the diamonds were annealed in vacuum ($\sim 10^{-6} \text{ Torr}$) with temperature $> 800^\circ\text{C}$. The NV densities for both samples were calibrated to be $\sim 0.5 \text{ ppm}$ using a spin-locking measurement [5].

IV. EXPERIMENTAL METHODS

IV.1. Experimental Details for Delta-Doped Sample S1

The delta-doped sample was mounted in a scanning confocal microscope. For optical pumping and readout of the NV centers, about $100 \mu\text{W}$ of 532 nm light was directed through an oil-immersion objective (Nikon Plan Fluor 100x, NA 1.49). The NV fluorescence was separated from the green 532 nm light with a dichroic filter and collected on a fiber-coupled single-photon counter. A magnetic field B was produced by a combination of three orthogonal electromagnetic coils and a permanent magnet. The field was aligned along one of the 100 crystal axes of the diamond sample and set to $B = 270 \text{ G}$, as calibrated via the spectrum of the NV centers. The microwaves used to drive magnetic dipole transitions for both NV and P1 centers were delivered via an Omega-shaped stripline with typical Rabi frequencies $\sim 2\pi \times 10 \text{ MHz}$.

IV.2. Experimental Details for Sample S2

Sample S2 was mounted in a confocal microscope. For optical initialization and readout, about $350 \mu\text{W}$ of 532 nm light was directed through an air objective (Olympus UPLSA 40x, NA 0.95). The NV fluorescence was similarly

separated from the 532 nm light with a dichroic mirror and directed onto a fiber-coupled avalanche photodiode. A permanent magnet produced a field of about 320 G at the location of the sample. The field was aligned along one of the NV axes, and alignment was demonstrated by maximizing the ^{15}N nuclear polarization [7]. Microwaves were delivered with a free-space rf antenna positioned over the sample.

IV.3. Experimental Details for Sample S3 and S4

Samples S3 and S4 were mounted in a confocal microscope. For optical initialization and readout, about 3 mW of 532 nm light was directed through an air objective (Olympus LUCPLFLN, NA 0.6). The NV fluorescence was separated from the 532 nm light with a dichroic mirror and directed onto a fiber-coupled photodiode (Thorlabs). The magnetic field was produced with an electromagnet with field strength ~ 174 G (~ 275 G) for sample S3 (S4). The field was aligned along one of the NV axes, and alignment was demonstrated by making the resonances from the other 3 NV axes degenerate. Microwaves were delivered using an Omega-shaped stripline with typical Rabi frequencies $\sim 2\pi \times 10$ MHz.

IV.4. Polychromatic Drive

The polychromatic drive was generated by phase-modulating the resonant P1 microwave tone [8]. A random array of phase jumps $\Delta\theta$ was pre-generated and loaded onto an arbitrary waveform generator (AWG) controlling the IQ modulation ports of a signal generator. The linewidth of the drive $\delta\omega$ was controlled by fixing the standard deviation of the phase jumps $\sigma = \sqrt{\delta\omega\delta t}$ in the pre-generated array, where $1/\delta t = 1$ GS/s was the sampling rate of the AWG. The power in the drive was calibrated by measuring Rabi oscillations of the P1 centers without modulating the phase, i.e. by setting $\delta\omega = 0$.

V. NORMALIZATION OF DECOHERENCE DATA

The coherence of the NV spins is read out via the population imbalance between $\{|0\rangle, |-1\rangle\}$ states. The measured contrast $\lesssim 8\%$ is proportional — *not* equal — to the normalized coherence $C(t)$. To see a physically-meaningful stretch power in our log-log plots of the data [Fig. 2, Fig. 3 in the main text], it is necessary to normalize the data by an appropriate value that captures our best approximation of the $t = 0$ time point for the DEER and spin echo measurements.

V.1. $t = 0$ measurement for samples S1, S3, and S4

For a given pulse sequence (e.g. Ramsey or spin echo) and fixed measurement duration t , we perform a differential readout of the populations in the $|0\rangle$ and $|-1\rangle$ spin states of the NV, which mitigates the effect of NV and P1 charge dynamics induced by the laser initialization and readout pulses. As depicted schematically in Fig. E2, we allow the NV charge dynamics to reach steady state (I) before applying an optical pumping pulse (II). Subsequently, we apply microwave pulses to both the NV and P1 spins (e.g. Ramsey or spin echo pulse sequences shown in Figs. 2-3 of the main text) (III). Finally, we detect the NV fluorescence (IV) to measure the NV population in $|0\rangle$, obtaining a signal S_0 . We repeat the same sequence a second time, with one additional π -pulse before detection to measure the NV population in $|-1\rangle$, obtaining a signal S_{-1} . The raw contrast, C_{raw} , at time t is then computed as $C_{\text{raw}}(t) \equiv [S_0(t) - S_{-1}(t)]$, and is typically $\lesssim 8\%$. We normalize the raw contrast to the $t = 0$ measurement to obtain the normalized coherence, $C(t)$, defined in the main text:

$$C(t) = C_{\text{raw}}(t)/C_{\text{raw}}(t = 0). \quad (\text{S1})$$

V.2. $t = 0$ Measurement for Sample S2

For sample S2, we have an early-time, rather than a $t = 0$, measurement at $t = 320$ ns for spin echo and DEER sequences. Because the DEER signal decays on a much faster timescale than the spin echo signal, we normalize both datasets to the earliest-time spin echo measurement.

VI. SPIN ECHO FOR SAMPLES S1 AND S2 WITHOUT POLYCHROMATIC DRIVING

In the section titled, *Characterizing microscopic spin-flip dynamics*, we discussed spin echo measurements limited—as one would naively expect—by NV-P1 interactions, and which exhibit an early-time stretch power of $\beta = 3D/2\alpha = 3/2$. These measurements were performed on samples S3 and S4 which exhibit a P1-to-NV density ratio of ~ 200 . By contrast, spin echo measurements in samples S1 and S2, with P1-to-NV density ratios of ~ 10 and ~ 40 , respectively, exhibit an early-time stretch $\beta = D/\alpha$ [Fig. E3], consistent with the prediction for a Ramsey measurement [Table 1 in the main text]. We note that here we are discussing a “canonical” spin echo measurement with no polychromatic drive [inset, Fig. 2(b) in the main text], and thus this data is not in contradiction with that presented in Fig. 3 of the main text.

A possible explanation for the observed early-time stretch $\beta = D/\alpha$ is that the spin echo signal is limited by NV-NV interactions, rather than by NV-P1 interactions. In order to understand this limitation, it is important to realize that the measured spin echo signal actually contains at least two contributions: (i) the expected spin echo signal from NV-P1 interactions, arising because the intermediate π -pulse decouples the NVs from any quasi-static P1 contribution; (ii) a Ramsey signal from NV interactions with other NVs, arising because these NVs are flipped together by the π -pulse, and the inter-group Ising interactions are not decoupled.

Two pieces of evidence support our hypothesis that NV-NV interactions limit the spin-echo measurement. First, for sample S1, fitting the XY-8 (directly characterizing the NV-NV interaction) [orange data, Fig. E1(a)] and spin echo signals [Fig. E3(a)] using χ^{DEER} yields the same fitted NV-NV correlation time $\tau_c^{\text{NV}} = 50 \mu\text{s}$, as well as similar (within a factor of two) $1/e$ decay timescales. Second, we have observed experimentally that two samples (S3, S4) with NV to P1 density ratios ~ 200 exhibit $\beta = 3D/2\alpha$, whereas three samples (S1, S2) with lower P1 to NV density ratios $\sim 10, 40$ respectively exhibit $\beta = D/\alpha$. While we have not studied the stretch power systematically as a function of the P1-to-NV density ratio, our four existing results agree qualitatively with our hypothesis.

VI.1. Data Analysis and Fitting: Fig. 3 of main text

We separate our discussion of the data analysis relevant to Fig. 3 of the main text into two parts: First, we discuss how comparing the $D = 2$ and $D = 3$ best-fits to the DEER measurements enable us to identify the dimensionality of the underlying spin system. Second, armed with the fitted dimensionality, we fit spin echo and DEER measurements simultaneously to Eqn. 5 of the main text to extract the correlation time τ_c of the P1 system. We note that, except for the $t = 0$ normalization point (Sec. V), we only consider data at times $t > 0.5 \mu\text{s}$ to mitigate any effects of early-time coherent oscillations caused by the hyperfine coupling between the NV and its host nitrogen nuclear spin.

VI.2. Determining the dimensionality of the system

In order to determine the dimensionality of the different samples S1 and S2, we focus on the DEER signal, where the stretch power is given by $\beta = D/\alpha$ in the early-time ballistic regime and $\beta = D/2\alpha$ in the late-time random walk regime. Employing both Gaussian and Markovian assumptions, a closed form for the decoherence can be obtained as [9]:

$$C^{\text{DEER}}(t) = e^{-A[\chi^{\text{DEER}}(t)]^{D/2\alpha}}, \quad (\text{S2})$$

where χ^{DEER} is defined in Eqn. 5 of the main text.

Armed with Eqn. S2, we consider the decoherence dynamics for different powers of the polychromatic drive for both $D = 2$ and $D = 3$ (with $\alpha = 3$, as per the dipolar interaction). We compare the reduced χ_{fit}^2 goodness-of-fit parameters for the two values of D , and demonstrate that stretch power analysis of the main text indeed agrees with the dimensionality that best explains the observed DEER data. Changing the dimension D does not change the number of degrees of freedom in the fit, so a direct comparison of χ_{fit}^2 is meaningful. Our results are summarized in Fig. E4, where we observe that for sample S1 indeed the $D = 2$ fitting leads to a smaller χ_{fit}^2 , while for sample S2 the data is best captured by $D = 3$ [Fig. E4]. Independently fitting both the extracted signal $C(t)$ as well to its negative logarithm $-\log C(t)$ yields the same conclusions. This analysis complements the discussion in the main text in terms of the early-time and late-time stretch power of the decay.

VI.3. Extracting the correlation time τ_c

Having determined the dimensionality of samples S1 and S2, we now turn to characterizing the correlation times of the P1 spin systems in these samples. To robustly extract τ_c , we perform a simultaneous fit to both the DEER signal with Eqn. S2 and the spin echo signal with

$$C^{\text{SE}}(t) = e^{-A[\chi^{\text{SE}}(t)]^{D/2\alpha}}, \quad (\text{S3})$$

assuming a single amplitude A and correlation time τ_c for both normalized signals. Here, $\chi^{\text{DEER/SE}}$ depends on τ_c as defined in Eqn. 5 of the main text.

In order to carefully evaluate the uncertainty in the extracted correlation time, we take particular care to propagate the uncertainty in the $t = 0$ data used to normalize the raw contrast, i.e. $C_{\text{raw}}(t = 0)$ [Sec. V]. Owing to the two normalization methods for samples S1 and S2 [Sec. V], we estimate the uncertainty in two different ways:

- For samples S1, S3, and S4, we consider fluctuations of the normalization value, $C_{\text{raw}}(t = 0)$, by $\pm 10\%$. This is meant to account for a possible effect of the hyperfine interaction in this data point, as well as any additional systematic error.
- For sample S2, we first compute a linear interpolation of the early time spin echo decoherence to $t = 0$. We then sample the normalization uniformly between this extrapolated value and the earliest spin echo value.

By sampling over the possible values of $C_{\text{raw}}(t = 0)$, we build a distribution over the extracted values of τ_c fitting to both the coherence, $C(t)$, and its logarithm, $-\log C(t)$. The reported values in Fig. 3(d, e) correspond to the mean and standard deviation evaluated over this distribution.

We end this section by commenting that, as the drive strength is reduced the spin echo signal looks increasingly similar to the undriven spin echo data [Fig. E3], i.e. the early time stretch changes from $\beta = 3D/2\alpha$ to $\beta = D/\alpha$; our explanation for this observed stretch is given in Sec. VI. The deviation from the expected functional form for the decoherence leads to a large uncertainty in the extracted correlation time. The data also deviates from the model for larger drive strengths, e.g. $\Omega = 2\pi \times 4.05$ MHz, $\delta\omega = 2\pi \times 20$ MHz, where our assumption that $\delta\omega \gg \Omega$ is no longer valid [Fig. E5].

-
- [1] Syntek, “Products-1: Various industrial diamonds,” .
- [2] K. Ohno, F. Joseph Heremans, L. C. Bassett, B. A. Myers, D. M. Toyli, A. C. Bleszynski Jayich, C. J. Palmström, and D. D. Awschalom, *Applied Physics Letters* **101**, 082413 (2012).
- [3] J. Choi, H. Zhou, H. S. Knowles, R. Landig, S. Choi, and M. D. Lukin, *Physical Review X* **10**, 031002 (2020).
- [4] L. T. Hall, P. Kehayias, D. A. Simpson, A. Jarmola, A. Stacey, D. Budker, and L. C. L. Hollenberg, *Nature Communications* **7**, 10211 (2016).
- [5] C. Zu, F. Machado, B. Ye, *et al.*, under review (2021).
- [6] T. R. Eichhorn, C. A. McLellan, and A. C. Bleszynski Jayich, *Phys. Rev. Materials* **3**, 113802 (2019).
- [7] V. Jacques, P. Neumann, J. Beck, M. Markham, D. Twitchen, J. Meijer, F. Kaiser, G. Balasubramanian, F. Jelezko, and J. Wrachtrup, *Phys. Rev. Lett.* **102**, 057403 (2009).
- [8] M. Joos, D. Bluvstein, Y. Lyu, D. M. Weld, and A. B. Jayich, “Protecting qubit coherence by spectrally engineered driving of the spin environment,” (2021), arXiv:2101.09654 [quant-ph].
- [9] See Supplemental Information at [URL will be inserted by publisher] for supporting derivations, including Refs. XXX.

VII. EXTENDED DATA

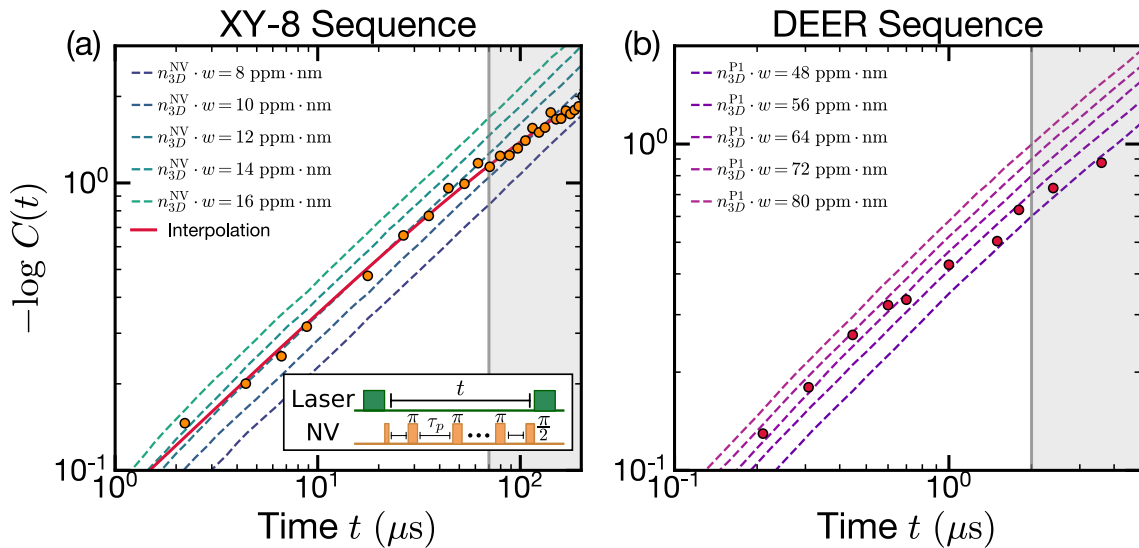


FIG. E1. We plot a set of numerically-computed curves (dashed lines) for early-time ballistic Ramsey decoherence caused by NV-NV interactions (a) and NV-P1 interactions (b), as a function of the NV areal density $n_{3D}^{NV} \cdot w$ and the P1 areal density $n_{3D}^{P1} \cdot w$, respectively. We compare these numerical results against the measured decoherence dynamics obtained via the XY-8 sequence (orange points, a) and the DEER sequence [after removing the NV contribution via the red interpolation in (a)] (purple points, b) to estimate the areal density of defects in sample S1. We estimate the areal density of NV centers to be $n_{3D}^{NV} \cdot w = 12 \pm 2$ ppm · nm and the P1 density to be $n_{3D}^{P1} \cdot w = 68 \pm 8$ ppm · nm. At late times (grey regions), the noise dynamics approach the incoherent random walk and should not be used to compute the density within this analysis. Inset in (a) shows XY-8 pulse sequence, with interpulse spacing τ_P .

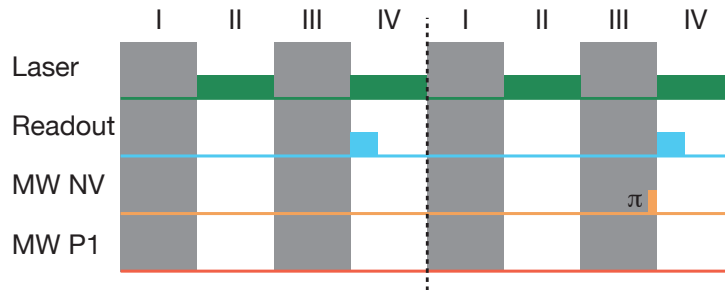


FIG. E2. Experiment sequence schematic for differential measurement.

Parameter	S1	S2	S3	S4
P1 Density	68(8) ppm · nm	20(1) ppm	~100 ppm	~100 ppm
NV Density	12(2) ppm · nm	0.43(1) ppm	~0.5 ppm	~0.5 ppm
Diamond cut	100	100	111	100
Nitrogen isotope	14	15	14	14
Isotopically purified?	Yes	Yes	No	No
Additional Comments	CVD grown	CVD grown, Ref. [6]	Type Ib, Ref. [5]	Type Ib
Field B	270 G	320 G	174 G	275 G
$\omega_{\text{NV}}/2\pi$	2.116 GHz	1.976 GHz	2.383 GHz	2.100 GHz
$\omega_{\text{P1}}/2\pi$	768 MHz	837 MHz	504 MHz	781 MHz

TABLE E1. Summary of experimental parameters.

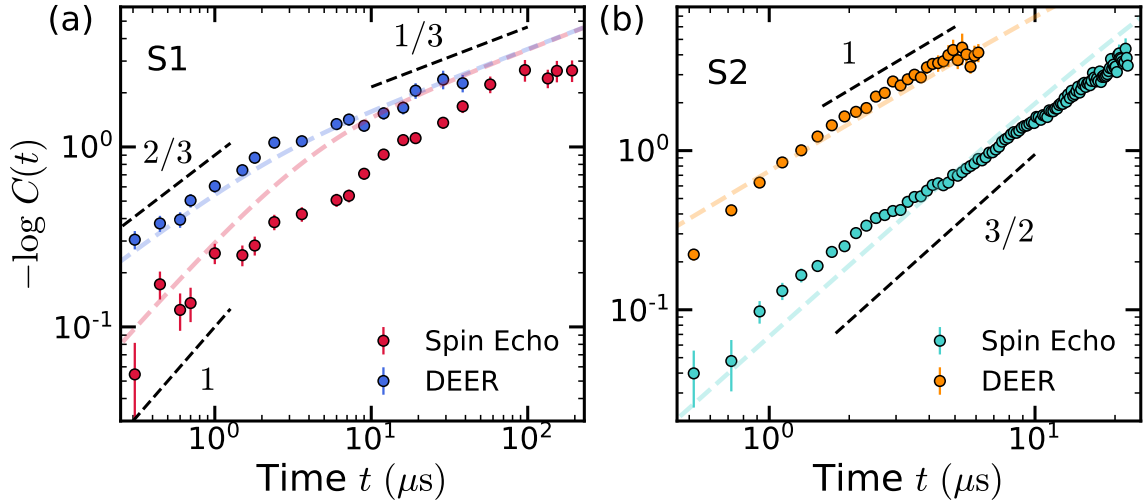


FIG. E3. Undriven DEER and spin echo data for sample S1 (a) and sample S2 (b). The DEER data is also plotted in Fig. 2(a) of the main text. The spin echo predictions (red, teal dashed curves) are computed from Eqn. S3, using the amplitude and correlation time of the fitted DEER curves (blue, orange dashed curves), but clearly disagrees with the data for both samples.

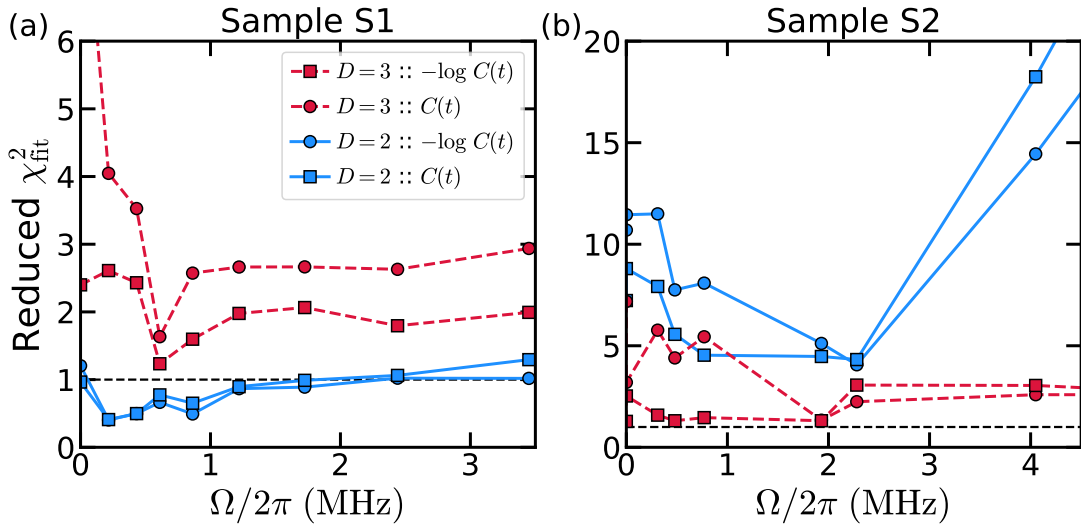


FIG. E4. Reduced χ_{fit}^2 for fits to the DEER measurements on samples S1 (a) and S2 (b) as a function of the incoherent driving strength, for four different fit models: we fit to both dimensions ($D = 2$ and $D = 3$) using the decoherence directly [$C(t)$] or its negative logarithm [$-\log C(t)$]. For samples S1 and S2, fits in both log and linear space show that $D = 2$ and $D = 3$ respectively better capture the data. The consistency of this result across a range of drive powers highlights our ability to distinguish the dimensionality of the sample directly from the decoherence dynamics.

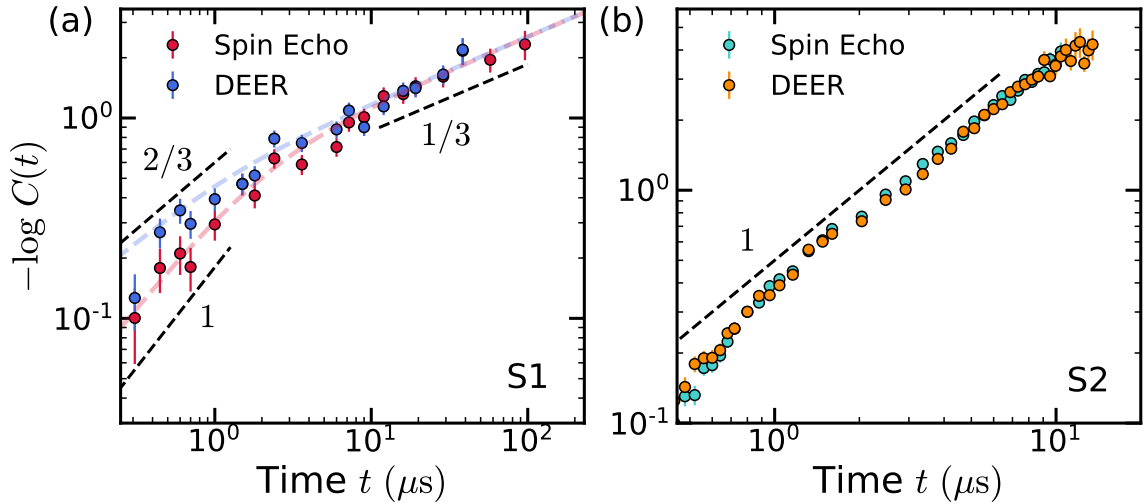


FIG. E5. DEER and spin echo for sample S1 (a) and sample S2 (b), under a fast incoherent drive ($\Omega = (2\pi) \times 3.45$ MHz and $\Omega = (2\pi) \times 4.05$ MHz, respectively). The data obtained for sample S2 plotted in (b) does not exhibit the correct “random-walk” regime stretch power of $1/2$, even though the DEER and spin echo signals overlap at all measured times.

Supplementary Information: Probing many-body noise in a strongly-interacting two-dimensional dipolar spin system

Emily J. Davis,^{1,*} Bingtian Ye,^{1,*} Francisco Machado,^{1,2,*} Simon A. Meynell,³ Thomas Mittiga,^{1,2} William Schenken,³ Maxime Joos,³ Bryce Kobrin,^{1,2} Yuanqi Lyu,¹ Dolev Bluvstein,⁴ Soonwon Choi,¹ Chong Zu,^{1,2,5} Ania C. Bleszynski Jayich,^{3,†} and Norman Y. Yao^{1,2,‡}

¹*Department of Physics, University of California, Berkeley, CA 94720, USA*

²*Materials Science Division, Lawrence Berkeley National Laboratory, Berkeley, CA 94720, USA*

³*Department of Physics, University of California, Santa Barbara, CA 93106, USA*

⁴*Department of Physics, Harvard University, Cambridge, MA 02138, USA*

⁵*Department of Physics, Washington University, St. Louis, MO 63130, USA*

I. ANALYTICAL DERIVATION OF THE DECOHERENCE PROFILE

Here, we provide additional details for the derivation of the results presented in the ‘‘Theoretical framework for decoherence dynamics induced by many-body noise’’ section of the main text. Let us recall the setup. Our system consists of a probe spin \hat{s}_p and a set of interacting system spins \hat{s}_i , coupled via long-range, $1/r^\alpha$, Ising interactions:

$$H_z = \sum_i \frac{J_z g_i}{r_i^\alpha} \hat{s}_p^z \hat{s}_i^z. \quad (\text{S1})$$

Here, we explicitly separate J_z as an overall constant interaction strength from any possible angular dependence g_i . We note that decoherence of the probe spin is due to spectral diffusion (i.e. dephasing) rather than depolarization, because the probe-system coupling includes no spin-exchange terms. This situation is natural in the NV-P1 systems used in our experiments, since the NV and P1 centers are far detuned and spin-exchange interactions are strongly suppressed [1].

We now proceed to derive the decoherence decay profile of the probe spins, first by treating the quantum operator \hat{s}_i^z as a classical variable s_i^z as in the main text. Later on, we will analyze the problem within a precise quantum description, and discuss the validity of different semi-classical approximations in different physical scenarios.

I.1. Average over trajectories

With a spin-1/2 probe initialized to point along the x -axis of the Bloch sphere, the coherence is simply defined as $C(t) = 2 \langle s_p^x(t) \rangle$. We apply a pulse sequence, such as Ramsey or spin echo, in which π -pulses applied to the probe spin effectively flip the sign of the Ising interaction, H_z ; let this sign be captured by the function $\eta(t'; t)$. For a particular $\eta(t'; t)$ applied on the probe spin up to the measurement duration t [Table S1], we then have

$$s_p^x(t) = \frac{1}{2} \text{Re} \left[e^{i \sum_i \frac{J_z g_i}{r_i^\alpha} \int_0^t \eta(t') s_i^z(t') dt'} \right]. \quad (\text{S2})$$

Explicitly, $\eta(t'; t)$ is the Fourier transform of the filter function $f(\omega; t)$ discussed in the main text. The phase

$$\phi(t) = \frac{J_z g_i}{r_i^\alpha} \int_0^t \eta(t') s_i^z(t') dt' \quad (\text{S3})$$

is a generalization of the phase $\phi(t)$ for a Ramsey sequence defined in the main text, which is obtained by setting $\eta(t') = 1$. The simplest case to treat analytically — although not necessarily the most physically relevant, as discussed

* Equal contribution

† ania@physics.ucsb.edu

‡ norman.yao@berkeley.edu

in the main text — is that of Gaussian-distributed phases $\phi(t)$. Making this approximation for now, we obtain

$$\langle s_p^x(t) \rangle = \frac{1}{2} \exp \left\{ -\frac{1}{2} \left\langle \left| \sum_i \frac{J_z g_i \int_0^t \eta(t') s_i^z(t') dt'}{r_i^\alpha} \right|^2 \right\rangle \right\} = \frac{1}{2} \prod_i \exp \left\{ -\frac{1}{2} \left[\frac{J_z |g_i| \chi(t)^{\frac{1}{2}}}{2r_i^\alpha} \right]^2 \right\}, \quad (\text{S4})$$

where

$$\chi(t) \equiv 4 \left\langle \left[\int_0^t \eta(t') s_i^z(t') dt' \right]^2 \right\rangle = \int_0^t dt' \int_0^t dt'' \eta(t') \eta(t'') \langle 4s_i^z(t') s_i^z(t'') \rangle. \quad (\text{S5})$$

We assume the system spins are independent, and include a factor of 4 in the definition of $\chi(t)$ to normalize the correlation function of spin-1/2 particles. To evaluate $\chi(t)$ analytically, we assume a Markovian form for the correlation function

$$\xi(t') \equiv \langle 4s_i^z(t_0) s_i^z(t_0 + t') \rangle = e^{-|t'|/\tau_c}, \quad (\text{S6})$$

where τ_c is the correlation time of the spins s_i , and we use the fact that $\langle 4s_i^z(t_0) s_i^z(t_0) \rangle = 1$ at infinite temperature. Depending on the specific pulse sequence applied on the bath spins (as captured by $\eta(t')$), we can analytically obtain the expression for $\chi(t)$, as shown in Table S1.

We note that Eqn. S5 can also be written in frequency space as:

$$\chi(t) = \int |f(\omega; t)|^2 S(\omega) d\omega, \quad (\text{S7})$$

where $f(\omega; t)$ and $S(\omega)$ are the Fourier transforms of $\eta(t'; t)$ and $\xi(t')$, respectively. The preceding analysis thus constitutes a derivation of Eqn. 2 of the main text.

Sequence	$\eta(t'; t)$	$\chi(t)$	Short-time $t \ll \tau_c$	Long-time $t \gg \tau_c$
Ramsey (DEER)	1	$2\tau_c t - 2\tau_c^2 \left(1 - e^{-\frac{t}{\tau_c}}\right)$	$t^2 - \frac{t^3}{3\tau_c}$	$2\tau_c t - 2\tau_c^2$
Spin Echo	$\begin{cases} 1 & 0 \leq t' < t/2 \\ -1 & t/2 \leq t' < t \end{cases}$	$2\tau_c t - 2\tau_c^2 \left(3 + e^{-\frac{t}{\tau_c}} - 4e^{-\frac{t}{2\tau_c}}\right)$	$\frac{t^3}{6\tau_c}$	$2\tau_c t - 6\tau_c^2$
XY-8	$\begin{cases} 1 & (m - \frac{1}{4})\tau_p \leq t' < (m + \frac{1}{4})\tau_p \\ -1 & (m + \frac{1}{4})\tau_p \leq t' < (m + \frac{3}{4})\tau_p \end{cases}$	$\frac{\tau_p^2}{12\tau_c} t$	$\frac{\tau_p^2}{12\tau_c} t$	$\frac{\tau_p^2}{12\tau_c} t$

TABLE S1. Expressions of $\eta(t'; t)$ and $\chi(t)$ for Ramsey/DEER, spin echo, and XY-8. In XY-8, we assume the inter-pulse spacing $\tau_p \ll \tau_c$.

I.2. Average over positional randomness

Assuming the P1 spins s_i occupy a total volume V , the average signal over positional disorder can be evaluated as follows [2]:

$$\begin{aligned}
\text{Signal} &= \frac{1}{2} \int \cdots \int \frac{d^D \vec{r}_1}{V} \frac{d^D \vec{r}_2}{V} \cdots \frac{d^D \vec{r}_N}{V} \prod_{i=1}^N \exp \left\{ -\frac{1}{2} \left[\frac{J_z |g_i| \chi(t)^{\frac{1}{2}}}{2r_i^\alpha} \right]^2 \right\} \\
&= \frac{1}{2} \left[\int \frac{d^D \vec{r}}{V} \exp \left\{ -\frac{1}{2} \left[\frac{J_z |g| \chi(t)^{\frac{1}{2}}}{2r^\alpha} \right]^2 \right\} \right]^N \\
&= \frac{1}{2} \left[1 - \frac{1}{V} \int \left(1 - \exp \left\{ -\frac{1}{2} \left[\frac{J_z |g| \chi(t)^{\frac{1}{2}}}{2r^\alpha} \right]^2 \right\} \right) d^D \vec{r} \right]^N.
\end{aligned} \tag{S8}$$

In the thermodynamic limit ($N, V \rightarrow \infty$ with fixed spin density $\frac{N}{V} = n$), we have

$$\begin{aligned}
\text{Signal} &= \frac{1}{2} \exp \left\{ -n \int \left(1 - e^{-\frac{1}{2} \left[\frac{J_z |g| \chi(t)^{\frac{1}{2}}}{2r^\alpha} \right]^2} \right) d^D \vec{r} \right\} \\
&= \frac{1}{2} \exp \left\{ -n \int \left(1 - e^{-\frac{1}{2} z^2} \right) r^{D-1} dr d\Omega \right\} \\
&= \frac{1}{2} \exp \left\{ -\frac{n}{\alpha} \left(\frac{J_z \chi^{\frac{1}{2}}}{2} \right)^{\frac{D}{\alpha}} \int \left(1 - e^{-\frac{1}{2} z^2} \right) z^{-\frac{D}{\alpha}-1} dz \int |g|^{\frac{D}{\alpha}} d\Omega \right\} \\
&= \frac{1}{2} \exp \left\{ -\frac{n D A_D}{\alpha} \left[-\frac{\Gamma(-\frac{D}{2\alpha})}{2^{\frac{D}{2\alpha}+1}} \right] \left[\frac{\bar{|g|} J_z \chi(t)^{\frac{1}{2}}}{2} \right]^{\frac{D}{\alpha}} \right\},
\end{aligned} \tag{S9}$$

where we make the substitution $z = \frac{J_z |g| \chi(t)^{\frac{1}{2}}}{2r_i^\alpha}$, $A_D = \frac{\pi^{\frac{D}{2}}}{\Gamma(\frac{D}{2}+1)}$ is the volume of a D -dimensional unit ball, and $\bar{|g|} = \left(\frac{\int |g|^{\frac{D}{\alpha}} d\Omega}{\int d\Omega} \right)^{\frac{\alpha}{D}}$ is the averaged angular dependence over a D -dimensional solid angle. The integral converges when $D < 2\alpha$, which agrees with the intuition that when $D \geq 2\alpha$, the effective long-range coupling decays so slowly that any resonance counting blows up.

Combining the results in Table S1 and Eqn. S9, we obtain the analytical form of the decoherence signal, averaged over the dynamical and positional randomness of the many-body system. In particular, for both the short-time and the long-time limits, the decay profiles are stretched exponentials, whose stretch powers and decay timescales are summarized in Table S2.

We note that the positional disorder is crucial in determining the shape of the decoherence decay profile. As highlighted by the difference between Eqn. S4 (excluding positional averaging) and Eqn. S9 (including positional averaging), the decay associated with a single spatial configuration is qualitatively different from the decay after averaging over positional disorder. Intuitively, each positional configuration has its own decay profile, and the experimental signal is an average over these different decays. At different times, the main contribution to the averaged signal can come from different positional configurations. For example, if different positional configurations exhibit exponential decays with different decay rates, then at short times those with fast decay rates dominate the averaged signal, but at long times those with slow decay rates become dominant. With this in mind, the coherence is determined by many different positional realizations, rather than the decay of a specific spatial configuration. By contrast, we note that if the bath spins are on a regular lattice, the decay profile follows the shape of the single positional realization case (Eqn. S4). In particular, for a regular lattice, the spin echo always decays as a stretched exponential with a stretch exponent of 3, independent of D and α .

	Profile	Stretch power	Decay timescale
Early-time Ramsey/DEER	$\exp \left[-n \left(C \bar{g} J_z t \right)^{\frac{D}{\alpha}} \right]$	$\frac{D}{\alpha}$	$(C \bar{g} n^{\frac{\alpha}{D}} J_z)^{-1}$
Early-time Echo	$\exp \left[-n \left(C \bar{g} J_z \sqrt{\frac{1}{6\tau_c}} t^{3/2} \right)^{\frac{D}{\alpha}} \right]$	$\frac{3D}{2\alpha}$	$(6\tau_c)^{\frac{1}{3}} (C \bar{g} n^{\frac{\alpha}{D}} J_z)^{-\frac{2}{3}}$
Late-time Ramsey/DEER and Echo	$\exp \left[-n \left(C \bar{g} J_z \sqrt{2\tau_c} t^{1/2} \right)^{\frac{D}{\alpha}} \right]$	$\frac{D}{2\alpha}$	$\left(\frac{1}{2\tau_c} \right) (C \bar{g} n^{\frac{\alpha}{D}} J_z)^{-2}$
XY8	$\exp \left[-n \left(C \bar{g} J_z \sqrt{\frac{\tau_p^2}{12\tau_c}} t^{1/2} \right)^{\frac{D}{\alpha}} \right]$	$\frac{D}{2\alpha}$	$\left(\frac{12\tau_c}{\tau_p^2} \right) (C \bar{g} n^{\frac{\alpha}{D}} J_z)^{-2}$

TABLE S2. Ensemble averaged decay profiles for Ramsey/DEER, spin echo, and XY-8 pulse sequences; $|\bar{g}|$ is the averaged angular dependence, and $C = \frac{1}{2} \left[-\frac{DA_D}{\alpha} \frac{\Gamma(-\frac{D}{2\alpha})}{\frac{D}{2\alpha} + 1} \right]^{\frac{\alpha}{D}}$ is a dimensionless constant only depending on D and α .

I.3. Quantum description

In the quantum description, the initial state of the full system (i.e. both the probe spin and the many-body system) is given by,

$$|\Psi_0\rangle = |\psi_0^s\rangle \otimes \left(\frac{|\uparrow\rangle + |\downarrow\rangle}{\sqrt{2}} \right), \quad (\text{S10})$$

where $|\psi_0^s\rangle$ is the initial state of the many-body system. The dynamics of the full system are governed by the time-dependent Hamiltonian, $H_{\text{tot}} = \eta(t')H_z + H_s$, where H_s is the Hamiltonian governing the intrinsic dynamics of the many-body system. After a measurement duration t , the initial state is transformed as

$$|\Psi(t)\rangle = \mathcal{T} e^{-i \int_0^t [\eta(t')H_z + H_s] dt'} |\Psi_0\rangle = \frac{(U_{\uparrow} |\psi_0^s\rangle) |\uparrow\rangle + (U_{\downarrow} |\psi_0^s\rangle) |\downarrow\rangle}{\sqrt{2}}, \quad (\text{S11})$$

where

$$U_{\uparrow} = \mathcal{T} e^{-i \int_0^t [\eta(t') \sum_i \frac{J_z g_i}{2r_i^{\alpha}} \hat{s}_i^z + H_s] dt'}, \quad U_{\downarrow} = \mathcal{T} e^{i \int_0^t [\eta(t') \sum_i \frac{J_z g_i}{2r_i^{\alpha}} \hat{s}_i^z + H_s] dt'} \quad (\text{S12})$$

are the evolution operators acting only on the system spins \hat{s}_i given the z -component of the probe spin. The coherence, $\langle \hat{s}_p^x \rangle$, corresponds to the overlap between the two evolution operators:

$$\langle \hat{s}_p^x \rangle = \text{Re}[\text{Tr}(U_{\uparrow} U_{\downarrow}^{\dagger})] / \mathcal{N}, \quad (\text{S13})$$

where \mathcal{N} is a normalization factor corresponding to the dimension of the system's Hilbert space.

Let us now move to the interaction picture by making the following substitution:

$$\begin{aligned} U_{\uparrow, \downarrow} &= U_0 \tilde{U}_{\uparrow, \downarrow} \\ U_0 &= \mathcal{T} e^{-i \int_0^t H_s dt'}. \end{aligned} \quad (\text{S14})$$

Then the two evolution operators and the decoherence signal become

$$\tilde{U}_{\uparrow, \downarrow} = \mathcal{T} e^{\mp i \int_0^t \eta(t') \sum_i \frac{J_z g_i}{2r_i^{\alpha}} \hat{s}_i^z(t') dt'} \quad (\text{S15})$$

$$\langle \hat{s}_p^x \rangle = \text{Re}[\text{Tr}(\tilde{U}_{\uparrow} \tilde{U}_{\downarrow}^{\dagger})] / \mathcal{N} = \text{Re}[\text{Tr}(\tilde{U}_{\uparrow}^2)] / \mathcal{N} \quad (\text{S16})$$

where

$$\hat{s}_i^z(t) = U_0^{\dagger}(t) \hat{s}_i^z(t) U_0(t). \quad (\text{S17})$$

The full quantum expression for the probe spin coherence $\langle \hat{s}_p^x \rangle$ obtained in Eqn. S16 provides several important insights

into the semi-classical approach we used in the main text and in the previous sections. First, Eqn. S16 is formally the same as Eqn. S2, except that $\hat{s}_i^z(t)$ is now a quantum operator. Second, assuming that different spins $\hat{s}_i^z(t)$ are independent, the problem reduces to an evaluation of the eigenvalues of the single spin evolution operator \hat{U}_\uparrow for each spin i independently.

While Eqn. S16 already averages over all possible initial states of both \hat{s}_i^z and its bath (i.e. other quantum degrees of freedom in H_s), one should also average the signal over the ensemble of the trajectories generated by the randomness of H_s (which arises, for example, from the polychromatic driving field, coupling to other classical degrees of freedom, positional and on-site disorder, etc.). This last point about two kinds of averages (one from different configurations of the many-body system and the other from the randomness of H_s) is essential for determining whether a telegraph or a continuous (Gaussian) random variable can better describe the many-body noise of \hat{s}_i^z . We note that, since the auto-correlator $\xi(t) \propto \langle \hat{s}_i^z(t) \hat{s}_i^z(0) \rangle$ always performs the two types of averages simultaneously, it does not contain the full information of the many-body noise.

I.4. Understanding decoherence dynamics in different physical scenarios

While Eqn. S15 provides the formula for the decoherence dynamics of a spin coupled to a dynamical bath, performing the necessary computation is intractable except in specific cases. In the following subsections, we describe two instructive examples where the explicit computation of Eqn. S15 can be performed and the relationship between the nature of the bath and the Gaussian or Telegraph noise is made clear.

Probe coupled to a single spin evolving under an external drive—First, we consider the case where the decoherence noise is generated by a single spin, whose dynamics are controlled by an external drive. In this case, the interaction Hamiltonian is given by:

$$H_s = \Omega[\hat{s}_i^x \cos \theta(t) + i \sin \hat{s}_i^y \theta(t)] \quad (\text{S18})$$

where Ω characterizes the strength of the drive and $\theta(t)$ is a time-dependent phase. The presence of such a time-dependent phase leads to the polychromatic drive described in the main text— $\theta(t)$ is chosen to follow a Gaussian stochastic process (see Methods, Sec. IV.4) [3], and is randomized across different runs of the experiment. Crucially, for each run of the experiment, the dynamics induced by H_s generate a particular trajectory around the Bloch sphere without any loss of single-particle coherence. As a result, the continuous spin rotation leads to a continuous change in the strength of the noise generated—this leads to the natural description of $s_i^z(t)$ as a continuous classical variable.

We emphasize that within this framework, there is a single phase accumulated due to the noise for the particular driving $\theta(t)$. As a result, to obtain a Gaussian distributed noise, one must additionally average over different driving $\theta(t)$. In the experiment this corresponds exactly to the polychromatic drive, where the phase of each experimental run is sampled from a Gaussian-Markov process.

Probe coupled to a strongly interacting system—We now turn to the opposite limit, where the dynamics of the system are strongly interacting. In this case, the dynamics of $\hat{s}_z^i(t)$ mirror that of a spin interacting with a large bath and the dynamics can be captured via the formalism of quantum jumps and the master equation. In particular, the dynamics of $\hat{s}_i^z(t)$ is similar to that of a spin undergoing spontaneous emission and absorption with a photon/phonon bath—starting in either the state $|\uparrow\rangle$ or $|\downarrow\rangle$, the system undergoes quantum jumps into the opposite state at a rate given by $1/\tau_c$ [4]. Eqn. S15 can then be obtained by computing the decoherence decay averaged over all the possible quantum jump trajectories—this precisely corresponds to a telegraph-like classical noise.

A few remarks are in order. First, we note that unlike the single driven spin case, the different trajectories within a single realization ensure that the phase accumulated already corresponds to a distribution and no additional averaging is necessary. This contrasts with the single spin example, where an explicit averaging over the driving fields was necessary to obtain the distribution of accumulated phases.

Second, this behavior can also be understood in the picture of the operator evolution described in Eqn. S15. Due to its coupling with the Markovian bath, the operator $\hat{s}_i^z(t)$ quickly spreads across a large number of degrees of freedom. As a result, the operators at different times commute with each other, i.e. $[\hat{s}_z^i(t), \hat{s}_z^i(t')] = 0$. This immediately leads to two consequences: 1) the time-ordering in Eqn. S15 is trivial and the eigenvalues of the exponential are the exponential of the eigenvalues of $\int_0^t \eta(t') \hat{s}_i^z(t') dt'$; 2) $\hat{s}_i^z(t)$ can be diagonalized simultaneously for all times. In this common eigenbasis, each eigenvector (labelled by μ) has a time-dependent eigenvalue $\lambda_\mu(t)$ corresponding to the time-dependent operator $\hat{s}_i^z(t)$, and eventually contributes an eigenvalue $\int_0^t \eta(t') \lambda_\mu(t') dt'$ to the spectrum of $\int_0^t \eta(t') \hat{s}_i^z(t') dt'$. Crucially, since $s_z^2(t) = 1/4$, $\lambda_\mu(t)$ can only be $\pm 1/2$ [5]. In this language, the decay of spin correlations $\langle \hat{s}_i^z(t) \hat{s}_i^z(t') \rangle \propto e^{-|t-t'|/\tau_c}$ is equivalent to the statement that the number of eigenvectors with $\lambda_\mu(t) = \lambda_\mu(t')$ decays

exponentially in time with rate $1/\tau_c$. Assuming that each eigenvector is independent, the associated eigenvalue $\lambda_\mu(t)$ follows a Poisson process and jumps between $\pm 1/2$. The dynamics of each $\lambda_\mu(t)$ can then be understood as either a single quantum jump trajectory (in the quantum language), or a single classical telegraph noise realization (in the classical description).

Spin coupled to a generic many-body system—Taking the above two examples into consideration, whether a generic many-body system is described by the Gaussian or the telegraph random variable is determined by the speed of the operator spreading. If the spreading of the operator is slow, the dynamics of $\hat{s}_z^i(t)$ remain constrained to a few sites throughout the measurement duration and the system appears coherent-like (leading to continuous Gaussian noise). If the spreading of the operator is fast, $\hat{s}_z^i(t)$ quickly spreads across many spins and the rest of the system acts as an effective Markovian bath, leading to telegraph noise.

In our disordered, strongly-interacting system, we conjecture that disorder leads to the slow spread of \hat{s}_z^i , and the decay of the auto-correlator $\langle \hat{s}_z^i(0)\hat{s}_z^i(t) \rangle$ mostly results from the different trajectories of local dynamics (originating from different H_s owing to different initial configurations of the bath spins). This is consistent with our experimental observation of the spin-echo decay stretch power $\beta = 3D/2\alpha$ for a three-dimensional dipolar ensemble, and is characteristic of the Gaussian noise model.

-
- [1] C. Zu, F. Machado, B. Ye, *et al.*, under review (2021).
 - [2] E. B. Fel'dman and S. Lacelle, *The Journal of chemical physics* **104**, 2000 (1996).
 - [3] M. Joos, D. Bluvstein, Y. Lyu, D. M. Weld, and A. B. Jayich, “Protecting qubit coherence by spectrally engineered driving of the spin environment,” (2021), arXiv:2101.09654 [quant-ph].
 - [4] P. Meystre and M. Sargent, *Elements of Quantum Optics*, 4th ed. (Springer-Verlag, Berlin Heidelberg, 2007).
 - [5] As long as the eigenspectrum of the original local operator is discrete, so will $\lambda_\mu(t)$; as a result, we expect the same telegraph noise description in the context of higher spin systems.